

Volume 6

Number 2

Apr - Jun 2017

STUDENT JOURNAL OF PHYSICS

INTERNATIONAL EDITION

INDIAN ASSOCIATION OF PHYSICS TEACHERS

ISSN – 2319-3166

STUDENT JOURNAL OF PHYSICS

EDITORIAL BOARD

Editor in Chief

L. Satpathy, Institute of Physics, Bhubaneswar, India
(satpathy@iopb.res.in)

Chief Editors

S. D. Mahanti, Physics and Astronomy Department,
Michigan State University, East Lansing, Mi 48824, USA
(mahanti@pa.msu.edu)

A.M. Srivastava, Institute of Physics, Bhubaneswar, India
(ajit@iopb.res.in)

INTERNATIONAL EDITORIAL BOARD

Danny Caballero, Department of Physics, Michigan State
University, U.S.A. (caballero@pa.msu.edu)

Gerd Kortemeyer, Joint Professor in Physics & Lyman
Briggs College, Michigan State University, U.S.A.
(kortemey@msu.edu)

Bedanga Das Mohanty, NISER, Bhubaneswar, India
(bedanga@niser.ac.in)

Prasanta Panigrahi, IISER, Kolkata, India
(panigrahi.iiser@gmail.com)

K.C. Ajith Prasad, Mahatma Gandhi College,
Thiruvananthapuram, India (ajithprasadkc@gmail.com)

Ralph Scheicher, Physics Department, University of
Uppsala, Sweden (ralph.scheicher@physics.uu.se)

Vijay A. Singh, Homi Bhabha Centre for Science Education
(TIFR), Mumbai, India (physics.sutra@gmail.com)

Allison Walker, Department of Physics, University of Bath
Bath BA2 7AY, UK (A.B.Walker@bath.ac.uk)

INTERNATIONAL ADVISORY BOARD

H.S. Mani, CMI, Chennai, India (hsmani@cmi.ac.in)

S. M. Moszkowski, UCLA, USA (stevemos@ucla.edu)

Jogesh C. Pati, SLAC, Stanford, USA
(pati@slac.stanford.edu)

Satya Prakash, Panjab University, Chandigarh, India
(profsprakash@hotmail.com)

T.V. Ramakrishnan, BHU, Varanasi, India
(tvrama@bhu.ac.in)

G. Rajasekaran, The Institute of Mathematical Sciences,
Chennai, India (graj@imsc.res.in)

Ashoke Sen, HRI, Allahabad, India (sen@hri.res.in)

X. Vinas, Departament d'Estructura i Constituents de la
Matèria and Institut de Ciències del Cosmos, Facultat de F
ísica, Universitat de Barcelona, Barcelona, Spain
(xavier@ecm.ub.edu)

Technical Editor

D. Pradhan, ILS, Bhubaneswar, India
(dayanidhi.pradhan@gmail.com)

Web Management

Aditya Prasad Ghosh, IOP, Bhubaneswar, India
(aditya@iopb.res.in)

Registered Office

Editor in Chief, SJP, Institute of Physics, Sainik
School, Bhubaneswar, Odisha, India - 751005

STUDENT JOURNAL OF PHYSICS

Scope of the Journal

The journal is devoted to research carried out by students at undergraduate level. It provides a platform for the young students to explore their creativity, originality, and independence in terms of research articles which may be written in collaboration with senior scientist(s), but with a very significant contribution from the student. The articles will be judged for suitability of publication in the following two broad categories:

1. **Project based articles**

These articles are based on research projects assigned and guided by senior scientist(s) and carried out predominantly or entirely by the student.

2. **Articles based on original ideas of student**

These articles are originated by the student and developed by him/ her with possible help from senior advisor.

Very often an undergraduate student producing original idea is unable to find a venue for its expression where it can get due attention. SJP, with its primary goal of encouraging original research at the undergraduate level provides a platform for bringing out such research works.

It is an online journal with no cost to the author.

Since SJP is concerned with undergraduate physics education, it will occasionally also publish articles on science education written by senior physicists.

Information for Authors

- Check the accuracy of your references.
- Include the complete source information for any references cited in the abstract. (Do not cite reference numbers in the abstract.)
- Number references in text consecutively, starting with [1].
- Language: Papers should have a clear presentation written in good English. Use a spell checker.

Submission

1. Use the link "[Submit](#)" of Website to submit all files (manuscript and figures) together in the submission (either as a single .tar file or as multiple files)
2. Choose one of the Editors in the link "[Submit](#)" of Website as communicating editor while submitting your manuscript.

Preparation for Submission

Use the template available at "[Submit](#)" section of Website for preparation of the manuscript.

Re-Submission

- For re-submission, please respond to the major points of the criticism raised by the referees.
- If your paper is accepted, please check the proofs carefully.

Scope

- SJP covers all areas of applied, fundamental, and interdisciplinary physics research.

Exploration of the Quantum Casimir Effect

A. Torode^{1**}

¹Department of Physics And Astronomy, 4th year undergraduate (senior), Michigan State University, East Lansing MI, 48823.

Abstract. Named after the Dutch Physicist Hendrik Casimir, The Casimir effect is a physical force that arises from fluctuations in electromagnetic field and explained by quantum field theory. The typical example of this is an apparent attraction created between two very closely placed parallel plates within a vacuum. Due to the nature of the vacuum's quantized field having to do with virtual particles, a force becomes present in the system. This effect creates ideas and explanations for subjects such as zero-point energy and relativistic Van der Waals forces. In this paper I will explore the Casimir effect and some of the astonishing mathematical results that originally come about from quantum field theory that explain it along side an approach that does not reference the zero-point energy from quantum field theory.

Keywords: Casimir effect, zero point energy, vacuum fluctuations.

1. INTRODUCTION AND HISTORY

The Casimir effect is a small attractive force caused by quantum fluctuations of the electromagnetic field in vacuum (Figure 1). In 1948 the Dutch physicist Hendrick Casimir published a paper predicting this effect [1, 2]. According to Quantum field theory, a vacuum contains particles (photons), the numbers of which are in a continuous state of fluctuation and can be thought of as popping in and out of existence [3]. These particles can cause a force of attraction. Most generally, the quantum Casimir effect is thought about in regards to two closely parallel plates. As the plates are brought together, Casimir realized that between them, only those virtual photons whose wavelengths fit a whole number of times should be counted whilst calculating the vacuum energy [1]. This leads to a decrease in energy density between the plates as they are moved closer which implies that a small force is drawing them together. similarly you can say that due to the smaller space between the plates only smaller exotic particles can exist between them. From this difference in particles outside the plates and those between the plates, a small pressure change can be calculated which creates a force pushing the plates towards one another [3]. This force is the Casimir effect.

In 1996, the small force was measured to within 5% uncertainty to that of the theoretical prediction by Steven Lamoreaux [4]. All bosons make a contribution to the Casimir force, but fermions make a repulsive contribution to the force. All of these particles make a contribution to the force though only that from photons is measurable. The theory states that the lowest energy state of a vacuum (the zero-point energy) is infinite when considering all possible photon modes. The original

** torodean@msu.edu

Casimir force derivation comes about from a situation in which the differences in infinities cancel out which arises from very interesting mathematics. There are inconsistencies and puzzles that arise from the existence of this effect, especially when applying it to the theories of quantum gravity. The solutions to these inconsistencies are however expected to be found within the solution to a theory of quantum gravity [1].

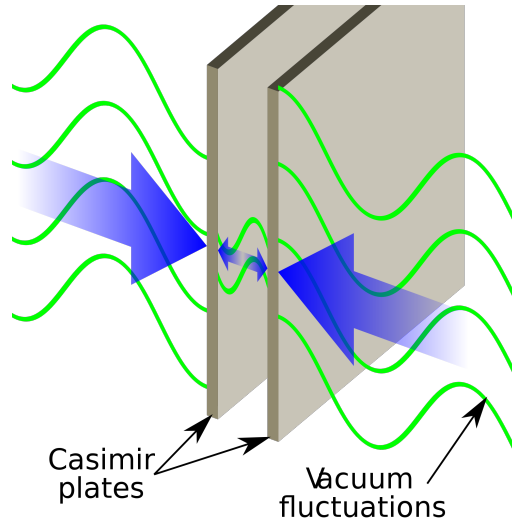


Figure 1. A simple diagram of two parallel plates and a representation of vacuum fluctuations [5].

In 2005, Jaffe made it clear that the zero-point fluctuations formulated in quantum field theory was not observable in any laboratory experiments though the vacuum value of the stress tensor (energy density of the vacuum) $\langle T_{\mu\nu} \rangle \equiv -\varepsilon g_{\mu\nu}$ even appears in the right hand side of Einstein's equation for gravity in general theory of relativity [6]

$$\frac{1}{2}g_{\mu\nu}R - R_{\mu\nu} = 8\pi G(\tilde{T}_{\mu\nu} - \varepsilon g_{\mu\nu}). \quad (1)$$

Jaffe also demonstrates in his paper that you can calculate the Casimir force without reference to the zero-point energy [6], which suggests that the zero-point energy may simply just be a nice mathematical construct in this situation to arrive at a measurable result. This will be discussed later in more detail.

2. 'ASTOUNDING' MATHEMATICAL RESULTS.

One of my favorite results I have encountered in my studies (which led me to the Casimir effect) follows as

$$\sum_{n=1}^{\infty} n \rightarrow -\frac{1}{12}. \quad (2)$$

This result does not explicitly make sense because the sum in equation (2) is a divergent sum. However, due to a process known as analytic continuation, some divergent sums can have a finite value. In 1913, this appeared in the work of a very famous mathematician from India, Srinivasa Ramanujan and is an important result for String Theory and other branches of physics. The Riemann zeta function

$$\zeta(s) = \sum_{n=1}^{\infty} \frac{1}{n^s} = 1 + 2^{-s} + 3^{-s} + 4^{-s} + \dots \quad (3)$$

is widely studied and used often in physics. In quantum physics, the energy density of a vacuum should be proportional to $\zeta(-3) = 1 + 8 + 27 + 64 + \dots$, which is a divergent series and thus does not make much sense as an energy density [7]. When we write this using equation (3) and use the process of analytic continuation, this can be written

$$\zeta(-3) = \sum_{n=1}^{\infty} \frac{1}{n^{-3}} = 1 + 2^3 + \dots \rightarrow \frac{1}{120}. \quad (4)$$

The way Ramanujan expresses functions that are divergent such as this (from the Riemann zeta function) is

$$\sum_{k=\alpha}^x f(k) \sim \int_{\alpha}^x f(t)dt + c + \frac{1}{2}f(x) + \sum_{k=1}^{\infty} \frac{B_{2k}}{(2k)!} f^{(2k-1)}(x), \quad (5)$$

[8]. This is a process of analytically continuing these divergent series and coming up with a finite result without any 'magic'. I say magic because there is a process in which one can ignore (in a sense) the divergent nature of a sum and come up with these results as well.

As an example, I will give a 'proof' of equation (2) using this method, which was first shown by Euler around 1735 [9]. Consider the following well defined sum

$$f(x) = 1 + x + x^2 + x^3 + x^4 + \dots = \frac{1}{1-x}, \quad (6)$$

for $|x| < 1$. Differentiating this gives

$$f'(x) = 1 + 2x + 3x^2 + \dots = \frac{1}{(1-x)^2}. \quad (7)$$

If we evaluate the result at $x = -1$ we get

$$f'(-1) = 1 - 2 + 3 - 4 + \dots = \frac{1}{4}. \quad (8)$$

Note that this is troublesome because we defined $f'(x)$ based on a function only valid for when $|x| < 1$. However, for our purposes suppose we can extend our limits and make $f(x)$ differentiable

A. Torode

at $x = -1$. Now, if we take $2^{-s}\zeta(s)$ we have

$$\begin{aligned} 2^{-s}\zeta(s) &= 2^{-s} \sum_{n=1}^{\infty} \frac{1}{n^s} = \sum_{n=1}^{\infty} \frac{2^{-s}}{n^s} \\ &= 2^{-s} + 4^{-s} + 6^{-s} + 8^{-s} \dots \end{aligned} \quad (9)$$

Now, if we take $g(s) = [1 - 2(2^{-s})]\zeta(s)$ we have

$$\begin{aligned} g(s) &= [1 - 2(2^{-s})]\zeta(s) \\ &= \zeta(s) - 2(2^{-s})\zeta(s) \\ &= 1 + 2^{-s} + 3^{-s} + 4^{-s} + 5^{-s} + 6^{-s} + \dots \\ &\quad - 2(2^{-s} + 4^{-s} + 6^{-s} + \dots) \\ &= 1 - 2^{-s} + 3^{-s} - 4^{-s} + 5^{-s} - 6^{-s} + \dots \end{aligned} \quad (10)$$

Finally, if we set $s = -1$, we can see that $g(-1) = \zeta(-1) - 2(2)\zeta(-1) = -3\zeta(-1)$ and evaluating this from equation (10) and then using our result from equation (8) gives us

$$\begin{aligned} -3\zeta(-1) &= 1 - 2 + 3 - 4 + \dots = \frac{1}{4} \\ \implies \zeta(-1) &= -\frac{1}{12}. \end{aligned} \quad (11)$$

Now, notice that plugging in $s = -1$ into the Riemann zeta function gives us the same result from equation (2) and thus

$$\zeta(-1) = -\frac{1}{12} \implies \sum_{n=1}^{\infty} n \rightarrow -\frac{1}{12}. \quad (12)$$

This result is very important to obtaining the $24 + 2 = 26$ dimensions in bosonic string theory [10]. It is also a simpler example than that of equation (4) to illustrate.

3. CASIMIR FORCE DERIVATION.

In Casimir's original paper, he did not use the result in equation (4) explicitly, though in a more recent derivation assuming zeta-regularization, one can see how it is obtained. Let k_x , k_y , and k_z represent the wave numbers in the x , y and z directions respectively. If we allow two plates to be parallel in the $x - y$ plane at a distance a apart, then we can define the cavity between the plates by

$$0 \leq x \leq \sqrt{A} \quad (13)$$

$$0 \leq y \leq \sqrt{A} \quad (14)$$

$$0 \leq z \leq a, \quad (15)$$

where the plates are a square of area A . If we adopt a periodic boundary condition, then we can show

$$k_x = \frac{2\pi n_x}{\sqrt{A}} \implies dn_x = \frac{\sqrt{A}}{2\pi} dk_x \quad (16)$$

$$k_y = \frac{2\pi n_y}{\sqrt{A}} \implies dn_y = \frac{\sqrt{A}}{2\pi} dk_y \quad (17)$$

$$k_z = \frac{n_z \pi}{a}, \quad (18)$$

with $(n_x, n_y, n_z) \in \mathbb{Z}$. The frequency of this wave is $\omega_n = v|\vec{k}| = v\sqrt{k_x^2 + k_y^2 + k_z^2}$. If we assume we are in a vacuum, then the speed of any electromagnetic wave is just c and thus $\omega_{n_z} = c\sqrt{k_x^2 + k_y^2 + k_z^2}$. The vacuum energy is the sum over all possible modes. The zero-point (ground state) energy associated with the n_z^{th} mode is given by $E_{n_z} = \frac{\hbar\omega_{n_z}}{2}$. The energy of all combined modes is then the sum over all n_z or $E = \sum_{n_z=1}^{\infty} \frac{\hbar\omega_{n_z}}{2}$. For simplicity we can allow $n \equiv n_z$. Taking the expectation value of the energy over the entire area of the plates can be done by integrating over all possible values of n_x, n_y and all possible expectation modes which yields

$$\langle E \rangle = \frac{\hbar}{2} \iint \sum_{n=1}^{\infty} \omega_n dn_x dn_y \quad (19)$$

$$= \frac{A\hbar}{8\pi^2} \iint \sum_{n=1}^{\infty} \omega_n dk_x dk_y. \quad (20)$$

This expression is clearly infinite due to the diverging sum. If we use zeta-regulation, we can find a finite energy per unit area by defining a quantity $\langle E(s) \rangle$ which goes to equation (20) when $s=0$.

$$\frac{\langle E(s) \rangle}{A} = \frac{\hbar}{8\pi^2} \iint \sum_{n=1}^{\infty} \omega_n |\omega_n|^{-s} dk_x dk_y \quad (21)$$

$$= \frac{\hbar}{8\pi^2} \sum_{n=1}^{\infty} \iint \omega_n |\omega_n|^{-s} dk_x dk_y. \quad (22)$$

Simplifying the above expression (Using Mathematica to take the integral over dk_x and dk_y) gives us

$$\frac{\langle E(s) \rangle}{A} = \frac{\hbar c^{1-s} \pi^{2-s}}{2a^{3-s} (3-s)} \sum_{n=1}^{\infty} |n|^{3-s}. \quad (23)$$

This may then be analytically continued to $s = 0$ where it becomes finite when using equation (4).

$$\frac{\langle E \rangle}{A} = \lim_{s \rightarrow 0} \frac{\langle E(s) \rangle}{A} = -\frac{\hbar c \pi^2}{6a^3} \zeta(-3). \quad (24)$$

Now, plugging in equation (4) in the above expression gives us

$$\frac{\langle E \rangle}{A} = \frac{-\hbar c \pi^2}{720a^3}. \quad (25)$$

A. Torode

The Casimir force per unit area between two parallel plates within a vacuum is therefore given by $F = -\nabla\langle E \rangle$ which is

$$\frac{F_c}{A} = -\frac{d}{da} \frac{\langle E \rangle}{A} = \frac{-\hbar c \pi^2}{240 a^4}. \quad (26)$$

As we can clearly see, this result would not have come about without the use of analytical continuation. In a sense, this is due to nature not containing apparent infinities. Rather, the continuation allowed us to arrive at a finite solution which is experimentally confirmed. The fact that our expression came out negative suggests that the force is an attractive force and due to the presence of \hbar , we can see that the force is of a quantum origin. In the original derivation, Casimir computed non-convergent sums using Euler-Maclaurin summation with a regularizing function [2].

4. IMPLICATIONS FROM THE ZERO-POINT DERIVATION.

The Casimir effect extends quantum field theory to allow for negative energy densities with respect to the ordinary vacuum energy. It has been suggested by numerous physicists such as Stephen Hawking, Kip Thorne, and many more that such a thing will allow the possibilities of stabilizing traversable wormholes [11]. Miguel Alcubierre, creator of the Alcubierre Drive has also suggested using the Casimir effect to obtain negative energy required for his designs [11]. In many cases, this effect has been shown to have possible applications in propulsion drives for space craft. It also has possible application in nanotechnology which has been suggested by some [11]. Due to the small scale that this force is observed on, this would make sense that it could present possible applications in nanotechnology. For instance, the force of attraction could be used as an architecture for moving components on a microscopic scale or something much more complex.

5. CASIMIR FORCE WITHOUT REFERENCING ZERO-POINT ENERGY.

As mentioned earlier, Jaffe argues that the Casimir force can be constructed without considering zero-point fluctuations of quantized electromagnetic field and is a result from the material of the plates and not resulting from zero-point energies. If we use the Drude model of metals, then the metal/conductor properties are characterized by a plasma frequency ω_p and a skin depth δ . The original result does not depend on anything other than the distance of the plates and fundamental constants. However, this result assumed that the plates were perfect conductors which do not exist in reality. The skin depth of a material is a measure of how far electromagnetic waves penetrate through a material and thus can cause a relationship between the waves within the plates to those outside.

Jaffe argues that both ω_p and δ are dependent on the fine structure constant α . He then argues that the perfect conductor approximation is good for sufficiently large α which in the case of the Casimir measurement scales for experimental verification are satisfied by the physical value of $\alpha \approx$

1/137 which is why the original derivation is supported by experimental results. Similarly, he also argues that the Casimir force vanishes as $\alpha \rightarrow 0$.

6. CONCLUSION

I have shown that while referencing zero-point energy one can derive the Casimir force using zeta-function regularization, however, it can also be calculated without reference to the zero-point energy which suggests that it may not be related to the energies that are suggested to come about from quantum field theory but instead the fine structure constant and properties of materials. It is fascinating to note that the same experimentally observed result can be obtained through a simple method using zeta-function regularization and ignoring divergences which may possibly suggest that this is a useful mathematical construct that could potentially have many real world applications. Much like the early use of imaginary numbers, which appeared to have no physical application, it may prove to be a useful method of mathematical manipulation that could lead us to new unique breakthroughs much like in the case of the Casimir force.

ACKNOWLEDGMENTS

This work was originally compiled as a poster presentation for a class project. I gratefully acknowledge the help of S.D Mahanti for suggesting I convert the project into this paper and proofreading/correcting my work. I would also like to acknowledge the help of C. Piermarocchi for assistance with the original project.

References

- [1] Gibbs, Philip. "What Is the Casimir Effect?" The Casimir Effect. University of California, 1997. Web. 16 Oct. 2016.
- [2] H.B.G. Casimir, Proc. Kon. Ned. Akad. Wetensch. B51, 793 (1948)
- [3] Casimir Effect & Black Holes - Sixty Symbols. Prod. Brady Haran. Perf. Mike Merrifield Ph.D. Youtube. University of Nottingham, 20 Mar. 2014. Web.
- [4] S. Lamoreaux, Phys. Rev. Lett. 78, 5 (1996)
- [5] Image from https://en.wikipedia.org/wiki/Casimir_effect
- [6] Jaffe. R. L. "Casimir effect and the quantum vacuum" 10.1103/PhysRevD.72.021301. 2005.
- [7] Berman, David. "Infinity or -1/12?" Plus.maths.org. +Plus Magazine, 18 Feb. 2014. Web. 16 Oct. 2016.
- [8] Library of Congress Cataloging in Publication Data Ramanujan Aiyangar, Srinivasa, 1887-1 920. Ramanujans notebooks. Mathematics-Collected works. 1. Berndt, Bruce C., 1939- II. Title. QA3. R33. 1985. 510. 84-20201
- [9] John Baez on the number 24. The Rankin Lectures 2008. Youtube. John Baez. University of California. 16 May. 2012. Web.
- [10] Sum of Natural Numbers (second proof and extra footage). Prod. Brady Haran. Perf. Ed Copeland Ph.D and Tony Padilla Ph.D. Youtube. University of Nottingham, 11 Jan. 2015. Wb.
- [11] Casimir effect. (n.d.). Retrieved October 16, 2016, from https://en.wikipedia.org/wiki/Casimir_effectcite_note-45

Solar wind and Sunspot variability in the 23rd and 24th solar cycles: A comparative analysis

M. Adhikary¹ and P.K. Panigrahi²

¹2nd year MS (Physical Science), Department of Applied Sciences, Gauhati University, Guwahati-781014, India.

²Department of Physical Sciences, Indian Institute of Science Education and Research, Kolkata, Mohanpur-741246, India

Email: adhikary.manashee@gmail.com, pprasanta@iiserkol.ac.in

Abstract: A comparative analysis of the stationary and non-stationary periodic variations of sunspot number and the solar wind flow speed is carried out for the 23rd and the 24th solar cycles. The variations of the sunspot number and solar wind speed at one AU distance from the Sun are identified through Fourier and Wavelet transforms. The former revealed significant inter and intra-cycle differences of the three dominant periodic components of durations 27, 13.5 and 9 days. The global Morlet wavelet spectra showed the stationarity of the dominant 27-day periodicity of the sunspot number and solar wind arising from Sun's rotation. The additional periodicities of 13.5-day and 9-day of the solar wind have non-stationary character, with strong intra cycle differences. Our analysis establishes correlation of topographical variation and spatial distribution of coronal holes with the fast components of the solar wind.

Keywords: Solar wind, Sunspot variability, Solar cycle, Wavelet transform

1. INTRODUCTION

Solar wind is a highly ionized magnetized plasma, originating from the Sun's corona and spread across a large volume known as the heliosphere, extending beyond the orbit of Pluto. Analysis of the periodic variations of solar wind (SW) in conjunction with the sunspot activity provides an ideal system for unravelling the dynamics of the fast and slow constituents of the solar wind and also the possible role of interplanetary medium where these two components interact. During a typical Solar cycle, darker regions known as "Sunspots" appearing from the relatively cooler regions of the solar photosphere, as a result of the periodic variation of the Solar magnetic field, pass a maximum-minimum-maximum phase in almost 11 years. The Solar wind parameters show signature of various high resolution periodicities, which can vary significantly in different cycles. In regions close to the Sun, SW consists of slow (~ 400 km/sec) and high speed (~ 750 km/sec) components, the former emanating from coronal holes and the latter possibly from the streamers [1]. During the period of a solar minima when the appearance of the Sunspots is minimal, large and stable coronal holes occur at the Sun's polar regions. They appear at lower latitudes during more active periods, which causes geomagnetic storms in the magnetosphere of Earth [2]. However, there is little understanding of the cause for the high velocity of the wind from these coronal gases [3]. Use of elemental abundances and freeze-in temperatures, as well as comparison of remote observations with in-situ properties

of solar wind have been proposed for tracing the sources of these two types of SW [4]. The study of SW behaviour in the interplanetary region is important for finding out the nature of interaction between high-speed and slow-speed components that alternately pass by Earth as the Sun rotates with a time-period of 27 days. Furthermore, SW has a significant effect on the space weather, making its study an area of active research [5], [6], [7]. Solanki et al. [8] have reconstructed sunspot number covering the past 11,400 years,

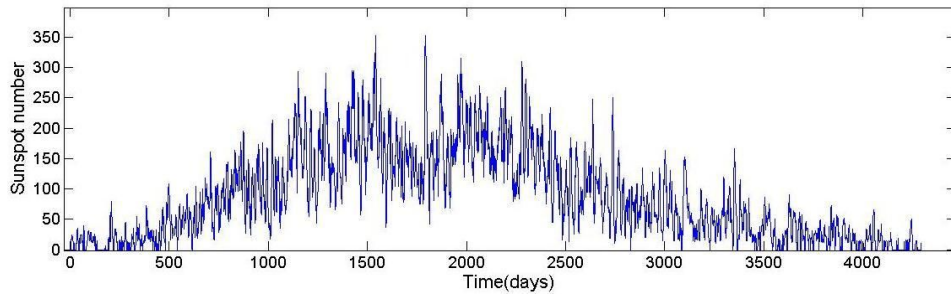


Figure 1: The daily sunspot number variation in the solar cycle 23, showing a double peak

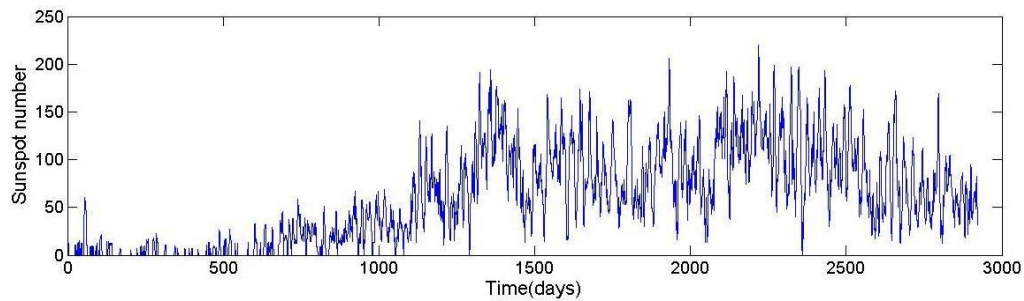


Figure 2: The daily sunspot number variation in the solar cycle 24, showing double peak structure

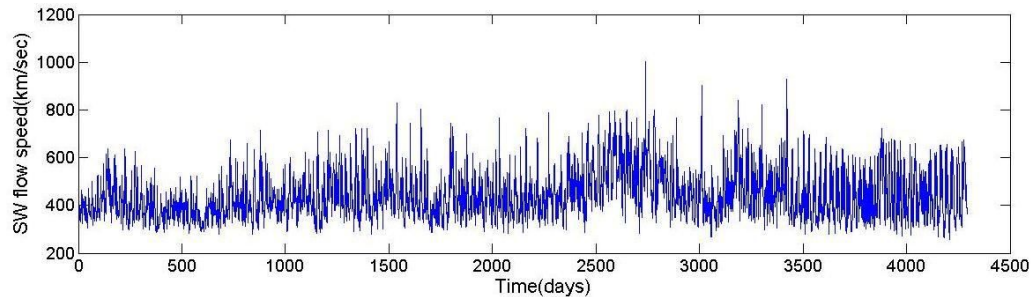


Figure 3: Time series plot of solar wind flow speed near 1 AU in the solar cycle 23

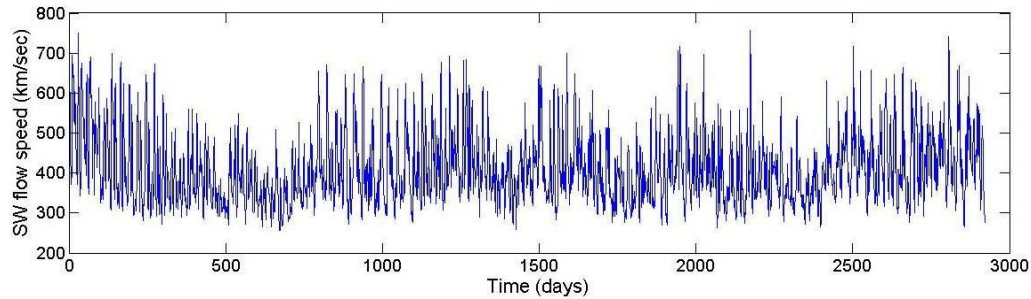


Figure 4: Time series plot of solar wind flow speed near 1 AU in the solar cycle 24

finding that the level of solar activity during the past 70 years has been exceptional. They also observed that the solar variability is unlikely to be the dominant cause for the recent unusual warming.

A recent study has showed that since mid 1990s, there has been a steady decline of the solar photospheric fields at latitudes $\geq 45^\circ$, as well as heliospheric microturbulence levels, [9] indicating weakening of the solar magnetic field. This is expected to affect the solar wind production and variability. The solar wind has strong impact on the terrestrial environment. Earth's thermosphere, extending about 60 to 300 miles above its surface, is constantly interacting with the solar wind. This interaction leads to density change of thermosphere that causes rise and fall of temperature, expanding and contracting on a 27-day period due to variation in extreme UV radiation. A systematic study showed that the periodic "breathing" of Earth's upper atmosphere is directly dependent on the solar wind variation [10]. It also indicated that high-speed wind from the sun triggers independent breathing episodes by creating geomagnetic disturbances. This atmosphere layer has periodic oscillation of 9 days, caused by the violent effect of the high-speed solar winds interacting with Earth's upper atmosphere. Both the sunspot activity and the SW variations are expected to vary in different cycles. The 23rd solar cycle, starting from mid 1996 and ending in the beginning of 2008, was a rather long one, lasting for 11.7 years, and a quiet one too. Currently, the 24th cycle is in progress since 4th January, 2008, having minimal activity until early 2010. According to the current predictions and observations, it is expected to be the smallest sunspot cycle since the cycle 14.

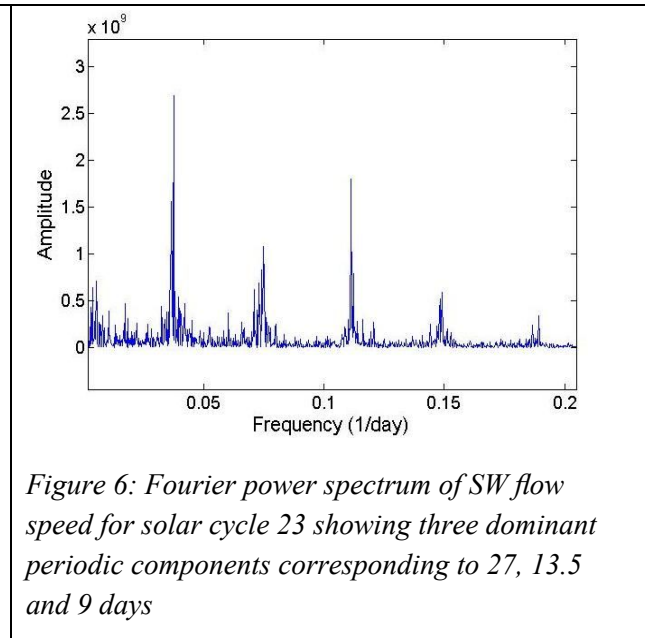
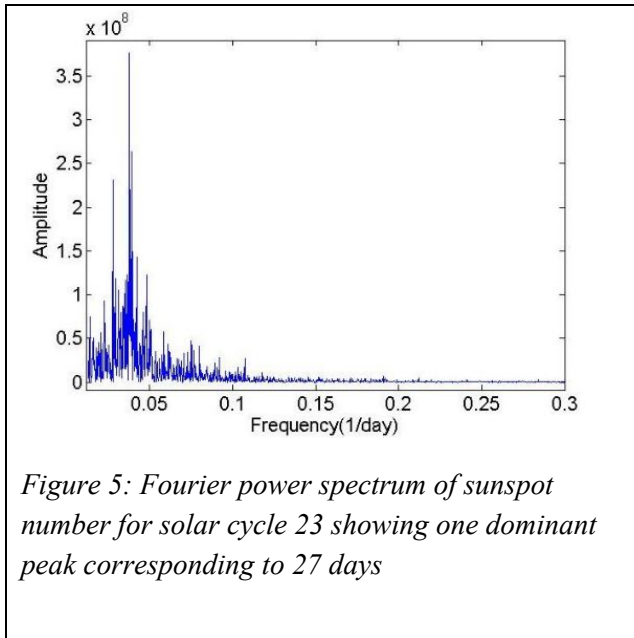
In the following, the 23rd and 24th cycles are studied, based on average solar wind speed as it reaches Earth's orbit, correlating with the variability in the sunspot number. We have collected 1-day resolution data from OMNIWeb data facility of NASA's SPDF Goddard Space Flight Centre, comprising of sunspot number and the solar wind flow speed (km/sec) near 1 AU from Sun, for both the cycles. *Figure 1* and *Figure 2* show the time-series plots of sunspot number respectively for the cycle 23 and 24 whereas *Figure 3* and *Figure 4* show the SW flow speed for the 23rd and 24th cycle for our analysis. Fourier transform is then used to find out hidden periodicities and to compare periodic variation of solar wind with the sunspot activity, and the nature of correlation of the periodic components in the 23rd and 24th cycles. For identification of time-frequency localization of the periodic variations, we apply Continuous Wavelet Transform (CWT) and

analyse global wavelet spectra with 95% confidence level. This shows the stationarity of the dominant periodicity and non-stationary nature of the other two variations of 13.5-day and 9-day periods.

2. FOURIER TRANSFORM ANALYSIS

Fourier transform is a convenient tool for identifying the presence of periodic behaviour in a time series [11], characterized by sharp peaks in the power spectrum. It splits a time domain signal ($f(t)$) to complex exponential functions of different frequencies [12],

$$F(\omega) = \int_{-\infty}^{\infty} f(t)e^{-i\omega t} dt$$



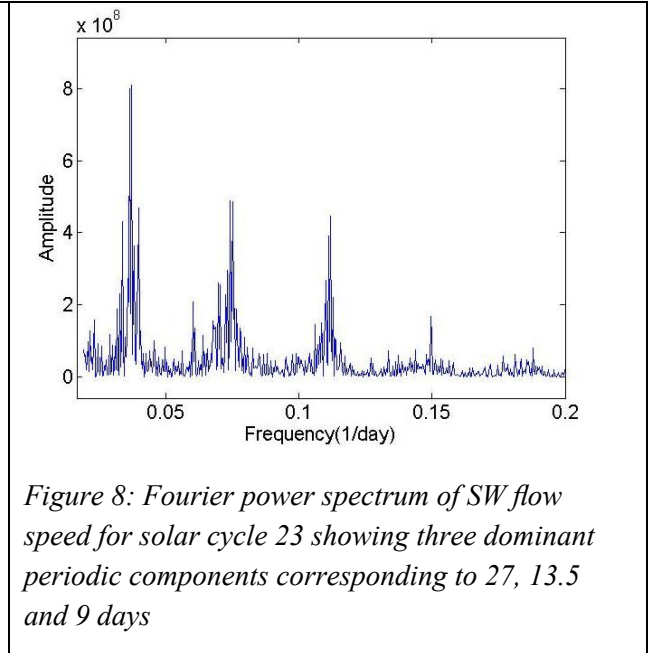
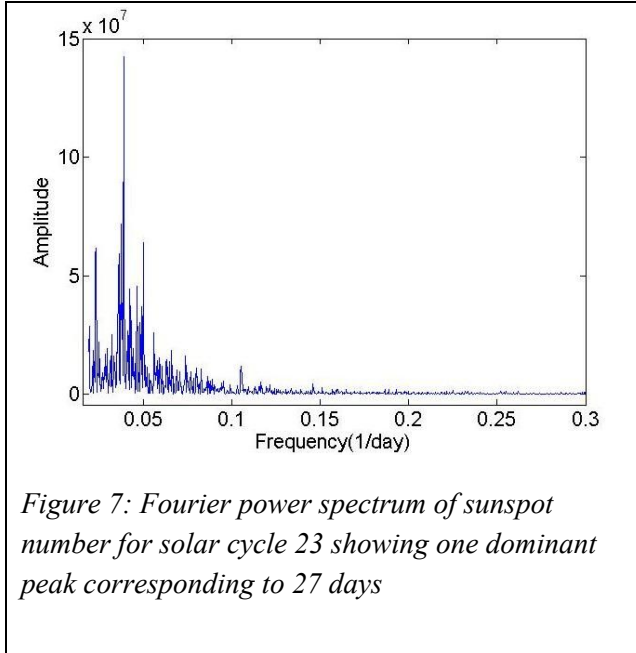


Figure 5 and Figure 6 depict Fourier transforms of the sunspot number and SW flow speed for the cycle 23, and Figure 7 and Figure 8 show the same for the cycle 24. The observed periodicities of solar wind match with previous studies. Periodicities of these two parameters, i.e., sunspot number variation and solar wind speed, show significant differences in both the cycles. The 27-day periodicity of sunspot activity clearly represents the solar rotation period, while the other higher resolution periodicities of 13.5-day and 9-days arise in solar wind speed which are absent in the sunspot number. Our Fourier spectra clearly reveals periodicities, from where, comparison of amplitudes of the Fourier powers also yields interesting inferences. Table 1 depicts amplitudes of Fourier powers for all the parameters considered for both the cycles. It can be observed that the Fourier amplitude of the 27-day periodic variation of sunspot number in 23rd and 24th cycles are quite comparable, implying same persistency of solar rotation period imposed on sunspot number variation. Solar wind, on the other hand, as it propagates towards earth shows signature of higher resolution periodicities of 13.5 and 9 days, with less amplitudes in case of cycle 24. Thus the 24th cycle is showing less stationarity

Table 1: Fourier amplitudes and periodicities

Parameter	Periodicity (days)	Fourier power (a.u.) (cycle 23)	Fourier power (a.u.) (cycle 24)
Sunspot Number	27	3.76×10^8	1.42×10^8
SW flow speed	27	2.69×10^9	8.08×10^8
	13.5	1.07×10^9	4.89×10^8
	9	1.80×10^9	4.46×10^8

of periodic behaviour along with less activity as compared to the former cycle. The significant difference in Fourier power for the two cycles implies variation in stationarity of the periodic modulations in SW speed. We therefore apply Continuous Wavelet Transform (CWT) for the visualization of time-frequency localization of these components, which is described in detail in the following section.

3. WAVELET TRANSFORM ANALYSIS

Wavelet transform may be considered as a mathematical microscope that reveals the behaviour of the signal in both time and frequency domain [13], [14]. This has to be compared with the Fourier transform, popularly called the ‘mathematical prism’, which reveals either the frequency or time variations. The "wavelet" is a small wave that has an oscillating wavelike characteristic and has its energy concentrated in time. Wavelet Transform (WT) makes it possible to use variable window sizes in analysing different frequency components within a signal or a time series, which is not permitted in case of Fourier Transform or even Short time Fourier Transform (STFT). When the given signal is compared with a set of functions obtained from the scaling and shift of a base wavelet, say "Morlet", the analysis is realized as shown in *Figure 9* [15].

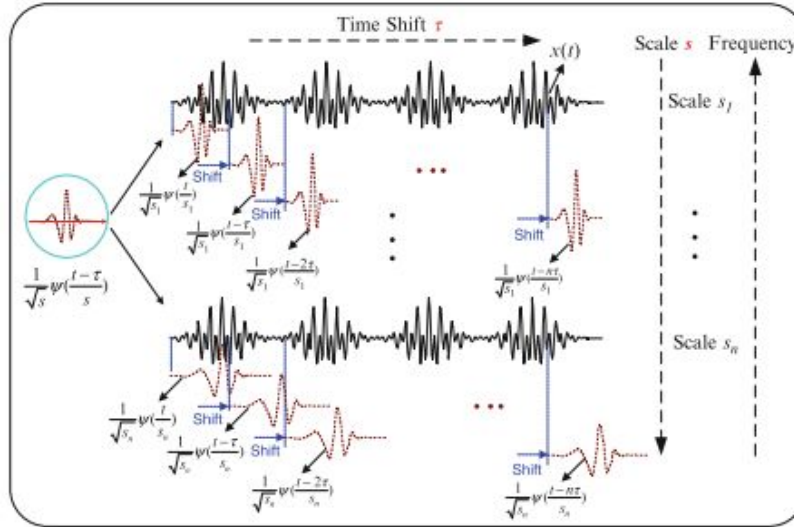


Figure 9: Wavelet Transform: enabling time-frequency analysis through different windows by scaling and shifting a base wavelet

Mathematically, Wavelet Transform (WT) can be expressed as

$$wt(s, \tau) = \langle x, \Psi_{s, \tau} \rangle = \frac{1}{\sqrt{s}} \int_{-\infty}^{\infty} x(t) \Psi^* \left(\frac{t-\tau}{s} \right) dt$$

and the variations of the time and frequency resolutions of the base wavelet, taken as Morlet wavelet here, at two locations on the time–frequency plane, $(\tau_1, \eta/s_1)$ and $(\tau_2, \eta/s_2)$ are depicted in the Figure 10 [15].

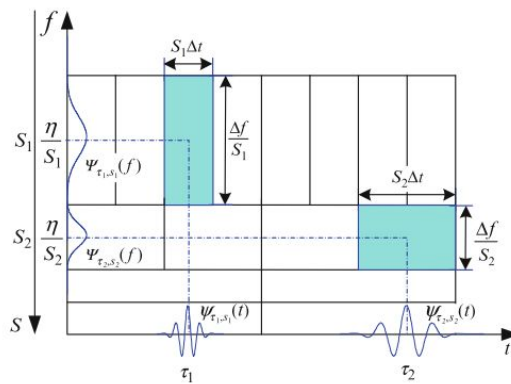


Figure 10: Variation of Morlet Wavelet in the time-frequency plane

By executing variations of the scale and time shifts of the base wavelet function intelligently, the WT can be used very effectively to extract the frequency components over the entire spectrum, by using small scales for decomposing high frequency parts and large scales for analysing the low frequency components.

The definition of the Continuous Wavelet Transform (CWT) may be found as

$$X(a, b) = \frac{1}{\sqrt{b}} \int_{-\infty}^{\infty} x(t) \Psi\left(\frac{t-a}{b}\right) dt$$

where 'a' shifts time, 'b' modulates the width (and not the frequency), and $\Psi(t)$ is the mother wavelet, which is taken as Morlet in the present work [16]. Morlet is a Gaussian windowed wavelet with sinusoidal modulations:

$$\Psi_0(t) = \pi^{-\frac{1}{4}} e^{i\omega_0 t} e^{-\frac{1}{2}t^2}$$

Here, ' ω_0 ' is dimensionless frequency and 't' is dimensionless time. The wavelet coefficients $C_{a,b}$ are then obtained from the convolution of data $f(t)$ with the wavelet $\Psi(t)$ as defined above, to come up with the net WT of the entire time series as a superposition of WT obtained from different windows used for the analysis. The dominant frequency components in the time series, at a particular instant of evolution, may thus be pinpointed by finding a higher value of this wavelet coefficient.

Figure 11 and *Figure 12* show CWT periodograms (global wavelet spectrum) of sunspot number and wind flow speed of cycle 23 and *Figure 13* and *Figure 14* show the same for cycle 24. While the x- and y- axes denote the time progression of the series and the scales used for localizing the analysis on the time-frequency plane, the magnitude of the wavelet coefficients is defined by the colour plot along the z-axis, red denoting highest and blue denoting lowest. The persistency of periodicities present in both the cycles can be clearly seen in this localized time-frequency plane analysis.

The 27-day periodicity is observed throughout the 11-year cycle of sunspot activity, whereas it is less stationary in flow speed along with additional 13.5-day and 9-day periodicities. The wavelet spectrum of solar wind speed in the 23rd cycle reveals that the 13.5-day periodicity is present in the declining phase when the Sunspot number comes down gradually from the Solar maximum.

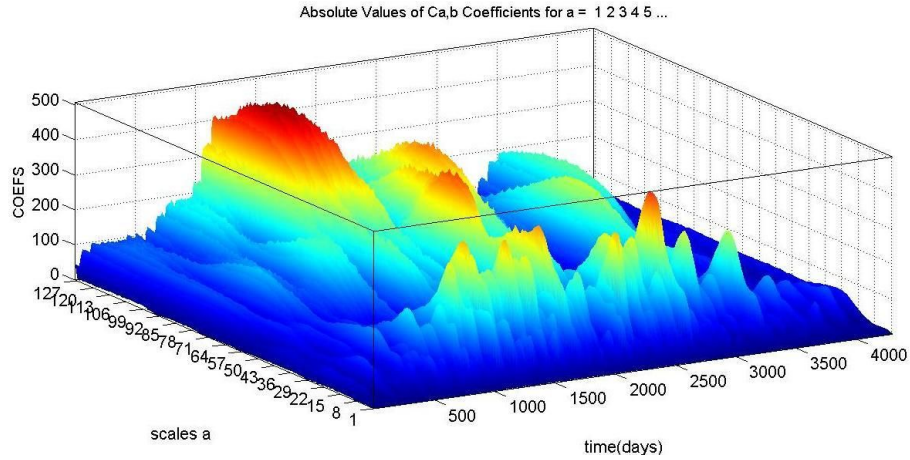


Figure 11: CWT periodogram of daily sunspot number for solar cycle 23, revealing stationary periodic variations corresponding to 27 days, while low frequency stationary noise too shows up during Solar maxima (middle portion)

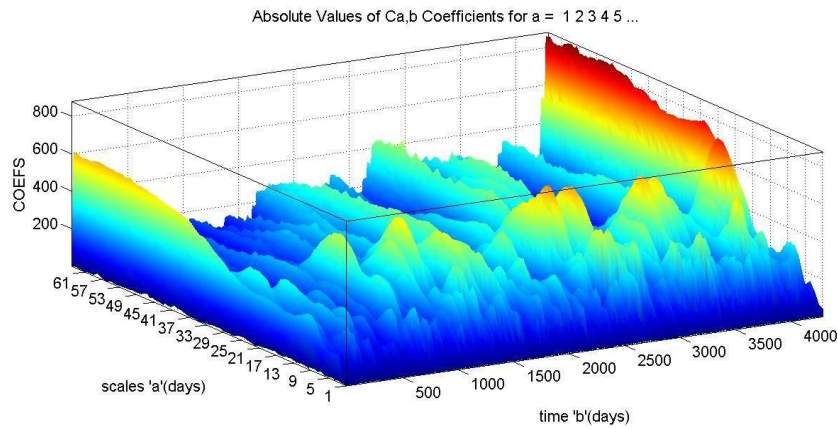


Figure 12: CWT periodogram of SW flow speed for solar cycle 23, revealing stationary and non-stationary periodic variations corresponding to 27, 13.5 and 9 days, while low frequency noise shows up during Solar minima (end portions)

The interaction of large-scale solar magnetic fields with the solar plasma leads to formation of coronal holes on the solar corona. These holes are said to have unipolar magnetic fields that open freely into the interplanetary medium, pushing fast streams of solar wind. During a solar cycle, coronal holes cover the polar regions during minimum activity, while they are distributed throughout all solar latitudes during more active periods, with less stability. Also, the coronal holes are more noticeable in the declining phase of the

solar cycle [17].

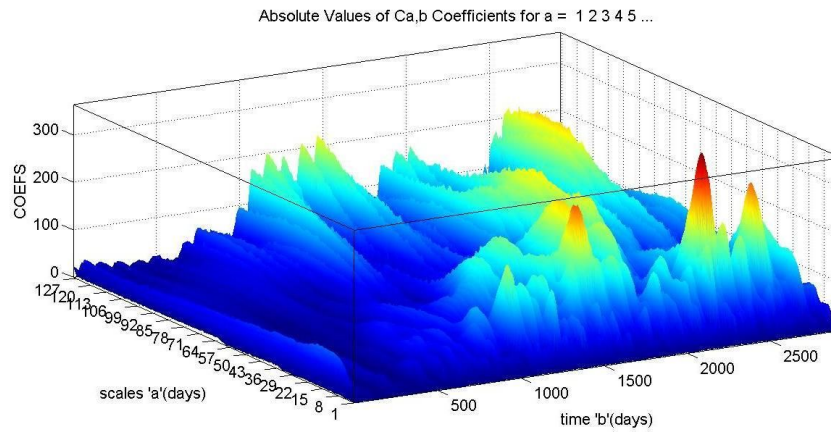


Figure 13: CWT periodogram of daily sunspot number for solar cycle 24, revealing stationary periodic variations corresponding to 27 days, while low frequency non-stationary noise shows up during Solar minima-maxima phase

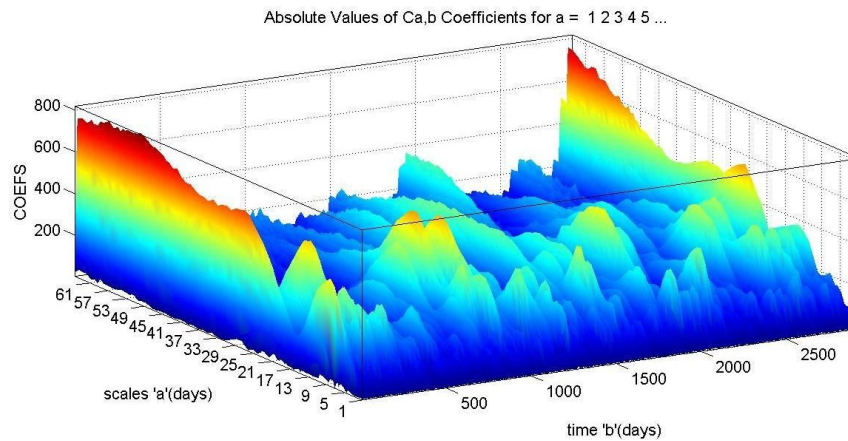


Figure 14: CWT periodogram of daily SW flow speed for solar cycle 24, revealing stationary and non-stationary periodic variations corresponding to 27, 13.5 and 9 days, while low frequency stationary noise shows up at Solar minima and nearby the Solar maxima

The stability of coronal holes may be inferred from the periodic variations of solar wind. The non-stationary 13.5-day and 9-day periodicity of solar wind speed arise due to the fast wind components, with speed more than 700 km/sec, the same being negligibly affected by the slow wind components. Our analysis shows that the 13.5-day and 9-day periodicities of solar wind speed at 1 AU arise because of the fast components of

solar wind. Hence, the periodic breathing of Earth's atmosphere, having the same periodicity is evidently caused by the fast winds, and hence has direct relation with spatial distribution of coronal holes. As it can be seen, the periodicity of 13.5-day and 9-day occur only in the case of solar wind, but not in solar surface activity. From the wavelet power spectra, it is evident that in the 23rd cycle, 9-day periodicity occur throughout the 11-year cycle, whereas the 13.5-day periodicity was observed only in the declining phase of the cycles. This may refer to two types of coronal holes, one being present almost over the whole cycle, whereas the other type appears in the declining phase. Drawing the same inferences for the 24th cycle is not convincing, since till now we are only halfway through it. The 13.5-day periodicity has been claimed to be due to two active solar longitudes approximately 180° apart, which occur around solar maxima [7] and have varying amplitudes in the two cycles. Similarly, the 9-day recurrence of fast solar wind streams originate from solar coronal holes distributed approximately 120° apart in longitude, and further transmitting its affect on modulating the terrestrial environment as it hit Earth every 9 days [18]

4. CONCLUSION

In conclusion, the present analysis of the solar wind speed near 1 AU provides insight into the association of coronal holes, existing due to differential rotation and tilted axis of rotation of the Sun, with the solar wind. The solar wind variability has been examined for cycle 23 and 24. The periodic variations for the 24th cycle shows lower power, indicating less stationarity in the 24th cycle as compared to the 23rd cycle. It may be attributed to the fact that this 24th cycle is yet to reach the half-way mark. The wavelet transform reveals the non-stationarity of these periodic components, manifested as the fast components in the solar wind during the minima-maxima phase of the Solar cycle, which affects Earth's atmosphere. Thus, it is proved that the spatial variation of coronal holes has important effect on solar wind periodicity at 1 AU. The obtained 13.5-day periodicity in the wind speed is due to the combined effect of solar rotation and the appearance of coronal holes 180° apart in longitude. In the global wavelet spectra of solar wind speed for both solar cycle 23 and 24, the 13.5-day periodicity can be observed, whose non-stationarity is dependent on the topological changes of these particular set of coronal holes. From this observation, we conclude that the appearance of 13.5-day period corresponds to the duration of appearance of the coronal holes, which has been possible to infer from an analysis of the wavelet spectra. In a similar manner, the 9-day period of solar wind can also be explained as a consequence of coronal holes situated at longitudes 120° apart. From the context of fast wind being emanating from coronal holes and the dependence of solar wind speed periodicity with the location of coronal holes, an important inference can be drawn that lower periods of 13.5-day and 9-days arise due to the fast components of solar wind which eventually comes from the coronal holes. The implication of this understanding on terrestrial atmosphere needs to be studied further.

ACKNOWLEDGEMENT

MA expresses sincere gratitude to Dr. Eeshankur Saikia for valuable discussions and much needed support while carrying out the work as well as in the preparation of the manuscript. MA also thanks the Department of Physical Sciences, IISER Kolkata, for giving the opportunity to carry out a part of this work there.

REFERENCES

- [1] J. L. Phillips, *Science*, p. 268, (1995).
- [2] J. T. Gosling, S. Bame, D. J. McComas and J. L. Phillip, *Geophys. Res. Lett.*, vol. 17, p. 901, (1990).
- [3] G. Poletto, *Journal of Advanced Research*, vol. 4, p. 215, (2013).
- [4] U. Feldman, E. Landi, and N. A. Schwadron, *J. Geophys. Res.*, vol. 110, p. 2156, (2005).
- [5] D. G. Cole, *Adv. Space Res.*, vol. 107, p. 295, (2003).
- [6] R. Schwenn, *Living Rev. Solar Phys*, vol. 3, (2006).
- [7] K. Mursula and B. Zieger, *J. Geophys. Res.*, vol. 101, (1996).
- [8] S. K. Solanki, I. G. Usoskin, B. Kromer, M. Schussler and J. Beer, *Letters to Nature*, vol. 431, (2004).
- [9] P. Janardhan, *J. Geophys. Res.*, vol. 120, (2015).
- [10] J. P. Thayer, J. Lei, J. M. Forbes, E. K. Sutton and R. S. Nerem, *J. Geophys. Res.*, vol. 113, (2008).
- [11] S. J. Schiff D. T. Kaplan T. Sauer P. So, E. Ott and C. Grebogi, *Phys. Rev. Lett.*, vol. 76, (1996).
- [12] K. C. S. Bochner, *Fourier Transforms*, Princeton University Press, (1949).
- [13] B. B. Hubbard, *The World According to Wavelets*, Wellesley, Massachusetts: AK Peters, (1997).
- [14] I. Daubechies, "Ten lectures on wavelets," in *CBMS-NSF Regional Conference Series in Applied Mathematics*, Philadelphia, (1992).
- [15] M. Akay, *Time Frequency and Wavelets in Biomedical Signal Processing*, Wiley-IEEE Press, (1997).
- [16] C. T. a. G. P. Compo, *Bulletin of the American Meteorological Society*, vol. 79, p. 61, (1998).
- [17] A. Kavanagh and M. Denton, *Astronomy and Geophysics*, vol. 48, p. 6.24, (2007).
- [18] J. Lei, J. P. Thayer, J. M. Forbes, E. K. Sutton, R. S. Nerem, *Geophys. Res. Lett.*, vol. 35, (2008).

Fourier Transform of Electric Signal using Kundt's Tube

S. Paul^{1*} and M. C. Gandikota^{2}**

¹5yr integrated M.Sc., Department of Physics, NISER, Bhubaneswar, India, 752050.

²5yr integrated M.Sc., Department of Physics, NISER, Bhubaneswar, India, 752050.

Abstract. An experiment to demonstrate the Fourier transform of an electric signal using the Kundt's tube is described. The results of finding the component frequencies and estimating the Fourier coefficients of electric signals composed of two sinusoidal waves is reported. Undergraduate students are expected to better relate to the abstract concept of a Fourier transform with the aid of such mechanical demonstrations.

Keywords: Kundt's Tube, Fourier transform.

1. INTRODUCTION

The mathematical technique of Fourier transform has ubiquitous usage in physics. To demonstrate Fourier transform, there are experiments available which use electronic circuits, computer programs[1],[2] and bass guitar strings[3]. In this paper, we present a *mechanical* means of physically realizing a Fourier transform.

A mechanical demonstration of a Fourier transform can be achieved using a Kundt's tube. Kundt's tube is a simple and an easily available apparatus in undergraduate teaching labs where it is used to measure the speed of sound. In this experiment, we use the resonance property of the Kundt's tube to find the frequencies and amplitudes of component sinusoidal waves which make up an electric signal.

2. THEORY

The representation of a function as a sum of sine and cosine terms is called a Fourier series[4]. That is to say, that the right hand side of

$$f(x) = \frac{a_0}{2} + \sum_{r=0}^{r=\infty} [a_r \cos(\omega_r x) + b_r \sin(\omega_r x)] \quad (1)$$

is the Fourier series of the function $f(x)$. a_0, a_r, b_r are called the Fourier coefficients of 'component' frequencies ω_r and can be mathematically calculated using the orthogonality properties of the above trigonometric functions.

Historically, Kundt (1866) had used the concept of stationary waves to measure the speed of sound with better accuracy[5]. Even to this day, we find this tube in undergraduate teaching labs

** s.paul@cyi.ac.cy, mgandiko@syr.edu

to introduce undergraduate students to one of the methods of measurement of speed of sound. The Kundt's tube resonates when sound waves of certain frequencies pass through it. For a tube closed at one end and the source at the other end, the resonating frequencies are,

$$\nu_n = \frac{2n + 1}{4} \frac{v_s}{L} \quad (2)$$

where L is length of tube, v_s is speed of sound in the medium encapsulated by tube and $n \geq 0$ is an integer.

3. APPARATUS

The setup consists of the Kundt's tube, a cork which is movable along the length of it and a speaker at other end. Cork dust or thermocol pieces are used as mediums for observing striations in the tube. Open source softwares, *Audacity* and *Praat* are used, for producing input signals and recording the signal from a microphone in the Kundt's tube respectively.

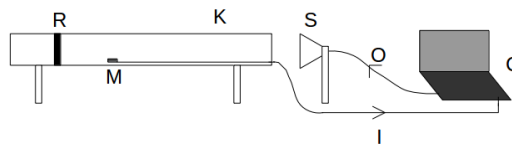


Figure 1. Schematic diagram of setup for the quantitative FT. **Legend** - R: Cork, K: Kundt's tube, M: Microphone, S: Speaker, C: Computer, I: Input from microphone, O: Output to speaker This Kundt's tube is closed only at one end as the air near the speaker-end forms an anti-node forced by the vibrations of speaker's diaphragm.

4. EXPERIMENT

Audacity is used to add two sinusoidal waves to make an electric signal which is then fed to the speaker. This electric signal is treated as a signal known to be composed of two sinusoidal waves but whose frequencies and amplitudes are unknown. The aim of the experiment is a primitive one: Decompose the electric signal to its component frequencies and amplitudes. The procedure for achieving the former and latter parts of this aim is presented in sections (4.1) and (4.2) respectively.

4.1 Qualitative Fourier Transform

The procedure to find the two unknown frequencies of the input signal will be referred to as the qualitative Fourier transform.

Before finding the component frequencies of the electric signal, a length-frequency calibration is necessary. The Kundt's tube is filled with an optimum amount of cork dust and the length of the tube is fixed by the cork. The resonant frequency for this length is estimated by feeding the

Fourier Transform of Electric Signal using Kundt's Tube

speaker a range of frequencies using a function generator and judging which frequency sets up the tallest striations in the cork dust. The resonant frequencies for a certain number of lengths are found similarly and plotted (Fig.(2)). Note that for the whole calibration, one should decide upon a single mode n . We chose $n = 1$ and selected frequencies which set up the corresponding pattern in the cork dust.

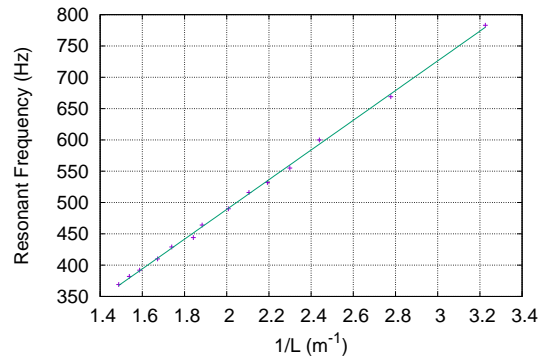


Figure 2. Length-Frequency calibration

Now, the speaker is fed with the unknown signal and the length of the cork is continually changed till the tube resonates at mode $n = 1$. This happens at two different lengths¹ which are noted. The resonant frequencies corresponding to these lengths is found using the calibration plot (2).

This concludes the qualitative Fourier transform as the two unknown frequencies that comprises the signal is found.

In the experiment that we performed, the electric signal fed to the speaker comprised of the frequencies: 358 Hz and 448 Hz and the qualitative FT found resonance at first mode at the lengths of 69 cm and 54 cm corresponding to the frequencies 358 Hz and 448 Hz.

4.2 Quantitative Fourier Transform

The procedure to find the amplitudes corresponding to the two unknown frequencies found using the qualitative FT will be referred to as Quantitative Fourier transform.

To quantify the Fourier transform, we need two more calibration curves. The cork is placed at one of the resonant lengths of the unknown signal and the cork-dust which has served its purpose is removed. A microphone is placed at the displacement anti-node. The speaker is fed with the corresponding resonant frequency at different input voltages using *Audacity* and the average sound

¹This is ensured only if the input signal's frequencies are in the range of frequencies covered in the calibration plot (2).

intensity measured using *Praat* is recorded for each input voltage. An average recorded intensity-input voltage calibration plot is thus obtained.

At this point, when we attempted to verify the shape of the waveform recorded by *Praat*, we found that the waveform was being truncated at the crests and troughs for high input voltages. To remove the associated errors in the average intensity recorded, we scaled down the volume in the computer appropriately.

Once the calibration for a particular resonant length is done, the same is repeated for the other resonant length. The calibration curves obtained are shown in Fig.(3).

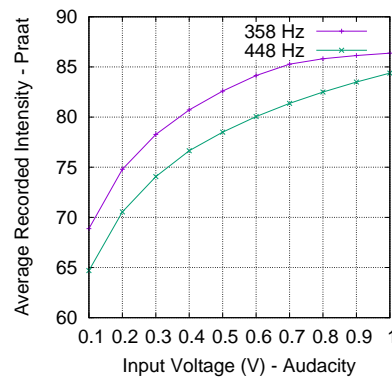


Figure 3. Recorded intensity-input voltage calibration

To find the amplitudes of the component frequencies of the electric signal, the Kundt's tube is kept at one of the resonant length and the microphone at the displacement anti-node. The unknown signal is fed to the speaker (at the same scaled down computer volume) and the average intensity is recorded. The corresponding input voltage is found using the calibration plots (3). Similar procedure is repeated for the other resonant length. Note that due to the scaling down of computer volume, the amplitudes here correspond to the scaled down electric signal and not the original electric signal which was used in Sec. (4.1).

This concludes the quantitative Fourier transform as the amplitudes of the two component frequencies are estimated.

In the experiment we performed, we fed these two frequencies at different pairs of amplitudes and the quantitative FT's estimated amplitudes are tabulated in Table.

5. DISCUSSION AND CONCLUSIONS

The complete process of finding out the component frequencies of an unknown input signal by scanning the length of Kundt's tube and estimating the amplitudes of the corresponding frequencies

Fourier Transform of Electric Signal using Kundt's Tube

using calibration curves can be referred to as taking the Fourier transform of an electric signal using Kundt's tube.

Like Kundt's tube, mechanical systems with discrete resonant frequencies can be considered as candidates for performing a Fourier transform of an electric signal. Once electric signals are transformed to mechanical signals, they can be fed to a resonance capable mechanical system. For example - springs of different resonant frequencies put on a hanger. A vibrator transforms electric signals to mechanical vibrations which are fed to the hanger and spring system. Only those springs whose resonant frequencies match with the frequency of the sinusoidal waves in electric signal will show resonance.

Though unnecessary for the present discussion, it is instructive to look at the Fourier transform that *Audacity* can perform on the sound signal recorded by the microphone when the speaker is fed with a sinusoidal resonant frequency of the tube. Fig.(4) shows such a plot where the speaker was fed with a 367Hz signal which was a resonant frequency for a particular length of the tube.

358 Hz					448 Hz			
Sl. No.	Input amp.(V)	Recd. av. intensity	Calib. reading	Error	Input amp.(V)	Recd. av. intensity	Calib. reading	Error
1	0.2	75.08	0.2	0	0.4	77.08	0.42	0.02
2	0.4	80.58	0.39	0.01	0.2	75.53	0.35	0.15
3	0.5	82.49	0.49	0.01	0.5	80.26	0.61	0.11
4	0.5	82.39	0.49	0.01	0.6	81.24	0.69	0.09
5	0.5	82.25	0.48	0.02	0.7	82.16	0.77	0.07
6	0.5	82.09	0.47	0.03	0.8	82.85	0.83	0.03
7	0.6	83.88	0.58	0.02	0.5	80.8	0.65	0.15
8	0.7	85	0.67	0.03	0.5	81.46	0.7	0.2
9	0.8	84.85	0.66	0.14	0.5	82.02	0.75	0.25
10	0.8	82.42	0.49	0.31	0.4	79.24	0.54	0.14
11	0.4	76.89	0.26	0.14	0.4	77.35	0.43	0.03
12	0.4	76.76	0.25	0.15	0.8	81.47	0.71	0.09

Table: The error tabulated is the difference between the expected value of amplitude measurement (Input Amplitude) and the measured amplitude (Calibration Reading). Excluding data points 8, 9 and 10, the error in amplitude measurements is less than 0.15 V.

It can be seen that though the speaker was fed with a single frequency, the constructive interference of certain frequencies contained in the noise are seen as peaks. These are different modes of resonance of the tube at that particular length.

As undergraduate students have better intuition towards sound waves as compared to electronic circuits or computer codes, we expect them to better relate to the meaning of Fourier transforms

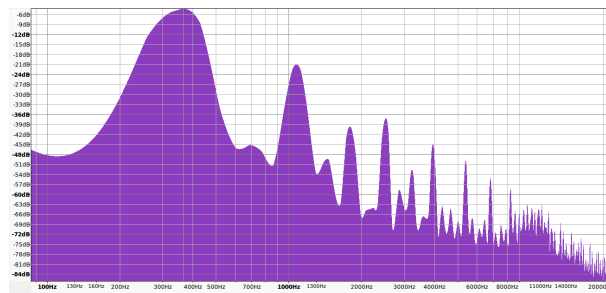


Figure 4. Recorded sound intensity versus frequency for input resonant signal: 367 Hz

with the aid of Kundt's tube.

ACKNOWLEDGMENTS

We thank Dr. K. Senapati for getting us to think of this problem. We acknowledge N. Anand for suggesting the Kundt's tube for performing a mechanical FT and Dr. R. Das for his encouragement. This experiment was funded by School of Physical Sciences, NISER - Bhubaneswar.

References

- [1] Lambert, Driscoll (1985) AJP 53, 874
- [2] www.teachspin.com/instruments/Fourier%20Methods/index.shtml
- [3] M. Courtney, N. Althausen (2006) *arXiv:physics/0605154* [physics.ed-ph]
- [4] Riley, Hobson Bence *Mathematical Methods for Physics and Engineering*, 3rd Ed. (Cambridge University Press, 2006)
- [5] A. Kundt (1866) *Annalen der Physik* (Leipzig: J. C. Poggendorff) 127 (4): p.497523

Decaying Dark Energy and Emergence of FRW Universe

Athira Sasidharan^{1*} and Titus K Mathew^{2**}

¹M.Sc Student 2011-13 Batch, Department of Physics, Cochin University of Science and Technology, Kochi-22, India

²Department of Physics, Cochin University of Science and Technology, Kochi-22, India.

Abstract. We consider a universe started in a de Sitter phase, with time varying holographic dark energy equivalent to a time varying cosmological term. The time varying dark energy and the created matter are consistent with the Einstein's equation. The general conservation law for the decaying dark energy and the created matter is stated. By assuming that the created matter is in relativistic form, we have analyzed the possibility of evolving the universe from de Sitter phase to Friedman-Robertson-Walker(FRW) universe.

Keywords: Dark energy, Friedmann Universe, Cosmology.

1. INTRODUCTION

Current astrophysical data shows that the present universe is accelerating in expansion[1]. This indicates that the present universe is dominated by some kind of very smooth form of energy with negative pressure and is called, dark energy, which accounts for about 73% of the total energy density of the present universe. Various models have been proposed to explain this phenomenon, for example there are models based on the dynamics of scalar or multi-scalar field, called quintessence models [2]. Another dark energy candidate is the cosmological constant, which was initially introduced by Einstein. In the cosmological constant model, the dark energy density, ρ_Λ , remains constant throughout the entire history of the universe, while the matter density decreases during the expansion. The equation of the state for cosmological constant as dark energy is $w = p/\rho_\Lambda = -1$. While in Phantom models [7], it is possible to have an equation of state with $w < -1$.

An alternative approach to dark energy is from holographic principle. According to the principle of holography the number of degrees of freedom in a bounded system should be finite and has relations with area of its boundary. By applying the principle to cosmology, one can obtain the upper bound of the entropy contained in the universe. For a system with size L and UV cut-off Λ , without decaying into a black hole, it is required that the total energy in a region of size L should not exceed the mass of a black hole of the same size, thus $L^3\rho_\Lambda \leq LM_P^2$. The largest L allowed is the one saturating this inequality, thus

$$\rho_\Lambda = 3c^2 M_P^2 L^{-2} \quad (1)$$

where c is numerical constant having value close to one, we will take it as one in our analysis. and M_P is the reduced Planck Mass $M_P^{-2} = 8\pi G$. When we take the whole universe into account, the

** tituskmathew@gmail.com, titus@cusat.ac.in

vacuum energy related to this holographic principle can be viewed as dark energy. L can be taken as the large scale of the universe, for example Hubble horizon, future event horizon or particle horizon which were discussed by many [5–9].

In this paper we assume a decaying cosmological term. We also assume that the universe is started in de-Sitter phase. While in the de-Sitter phase the universe is completely dominated with the cosmological term. As the universe expands the dynamical cosmological term decaying in to matter and the universe will subsequently enter the Friedman phase. As it expands further, the universe enter a matter dominated phase with decelerated expansion. In section two we have shown that the decaying cosmological dark energy and created matter are consistent with the Einstein’s equation. In section 3, we have obtained the Friedmann equations for the decaying dark energy, and analyzed the possibility of the evolution of the universe in to the Friedmann phase. We have also obtained the time evolution of the decaying dark energy and its equation of state. In section 4, we presented a comprehensive discussion of our analysis.

2. DYNAMICAL DARK ENERGY AND HORIZON

In the presence of cosmological constant the Einstein’s field equation is

$$G^{\mu\nu} = R^{\mu\nu} - \frac{1}{2}Rg^{\mu\nu} = \frac{8\pi G}{c^4}T_{total}^{\mu\nu} \quad (2)$$

where $G^{\mu\nu}$ is the Einstein tensor, $R^{\mu\nu}$ is Ricci tensor, R is the Ricci scalar (except in this equation, we will refer R as the scale factor of the expanding universe) and $T_{total}^{\mu\nu}$ is the total energy momentum tensor comprising matter and cosmological term, and is

$$T_{total}^{\mu\nu} = T^{\mu\nu} + \rho_{\Lambda}g^{\mu\nu} \quad (3)$$

in which $T^{\mu\nu}$ is the energy momentum tensor due to matter in perfect fluid form and ρ_{Λ} is the density due to cosmological term, given as,

$$\rho_{\Lambda} = \frac{c^4\Lambda}{8\pi G} \quad (4)$$

with Λ as the so called “cosmological constant”.

Einstein’s equation satisfies the covariant conservation condition,

$$\nabla_{\mu}G^{\mu\nu} = 0 \quad (5)$$

In the conventional case this implies that, $\nabla_{\mu}T^{\mu\nu} = 0$. As such this condition doesn’t give any time conserved charge. If the matter is being created from an independent source, say from the cosmological term, the conservation law will then take the general form

$$\nabla_{\mu}(T^{\mu\nu} + \rho_{\Lambda}g^{\mu\nu}) = 0 \quad (6)$$

This conservation law implies that the energy and momentum of matter alone is not conserved, but energy and momentum of matter and cosmological term or dark energy are together be conserved.

This general conservation law allows the exchange of energy and momentum between matter and dark energy. It is acting as a controlling condition for this exchange. The existing theories predicts a very large value for the cosmological term [3, 4] in the early stage of the universe, but the present observations points towards a very low value for the cosmological term for the late universe. In this light it is inevitable to consider that, there must be a transference of energy form the dark energy or cosmological term sector to the matter sector.

Let us assume that, the term Λ correspondingly ρ_Λ is a function of time, since a space dependent Λ will lead to an anisotropic universe. The covariant conservation law will then give the equations,

$$\nabla_\mu T^{\mu i} = 0 \quad (7)$$

and

$$\nabla_\mu T^{\mu 0} = -\frac{c^3}{8\pi G} \frac{d\Lambda}{dt} \quad (8)$$

where $i = 1, 2, 3$ for the spatial part and $i = 0$ for the time part.

In reference [10] authors have considered the energy transference between decaying cosmological term and matter. It is important to realize that the covariant conservation law given above is drastically different from that appearing in some quintessence model [11–13], where energy-momentum tensor of the scalar field that replaces the cosmological term is itself covalently conserved, but no matter creation. In the present paper we have considered that the cosmological term decaying into matter and is consistent with the Friedmann model of the universe.

The energy density ρ_Λ corresponds to the time varying cosmological term is taken as the holographic dark energy as defined in equation (1). A simple holographic dark energy model by taking $L = H^{-1}$, where H is the Hubble's constant was considered by Hsu et al [5] and they have shown that the Friedmann model with $\rho_\Lambda = 3c^2 M_p^2 H^2$ makes the dark energy behave like ordinary matter rather than a negative pressure fluid, and prohibits accelerating expansion of the universe. We adopt an equation for holographic dark energy energy, where the future event horizon (R_h) is used instead of the Hubble horizon as the IR cut-off L , which was shown to lead a accelerating universe by Li [14]. Thus the time varying cosmological energy density is

$$\rho_\Lambda = 3c^2 M_p^2 R_h^{-2} \quad (9)$$

where c is a constant with value $O(1)$ and the event horizon $R_h(t)$, a function of cosmological time, is given by

$$R_h(t) = R(t) \int_t^\infty \frac{dR(t')}{H(t')R(t')^2} \quad (10)$$

where $R(t)$ is the expansion factor and $H(t)$ is the Hubble constant.

3. COSMIC EVOLUTION OF DARK ENERGY AND FRIEDMANN UNIVERSE

Let us consider an empty universe in de Sitter phase, with very large [15] decaying cosmological term, corresponds to dark energy density as given by equation (9). If the matter from the decaying

dark energy, are themselves distributing in a homogeneous and isotropic manner, then the geometry of the universe can be taken to be of Friedmann-Robertson-Walker form,

$$ds^2 = c^2 dt^2 - R^2 \left[\frac{dr^2}{1 - kr^2} + r^2 (d\theta^2 + \sin^2 \theta d\phi^2) \right] \quad (11)$$

where k is the curvature parameter R is the scale factor of expansion, t is the cosmological time and (r, θ, ϕ) are the co-moving coordinates. By taking the energy momentum tensor of matter as

$$T_{\nu}^{\mu} = (\rho + p)u^{\mu}u_{\nu} - p\delta_{\nu}^{\mu} \quad (12)$$

where ρ is the energy density of the created component due to the decay of cosmological term and p is it's pressure. Under these conditions, the covariant conservation law (8) leads to (here we consider only one component of matter)

$$\frac{d\rho_m}{dt} + 3H(\rho_m + p_m) = -\frac{d\rho_{\Lambda}}{dt} \quad (13)$$

where $H = \frac{dR}{dt}/R$ is the Hubble parameter, ρ_m is the density of the created matter and p_m is its pressure. This equation obtained from the general conservation law is found to be followed from the combinations the standard Friedmann equations,

$$\left(\frac{dR}{dt}\right)^2 = \frac{8\pi G}{3c^2}(\rho_m + \rho_{\Lambda})R^2 - kR^2 \quad (14)$$

and

$$\frac{d^2R}{dt^2} = \frac{8\pi G}{3c^2} \left(\rho_{\Lambda} - \frac{1}{2}(\rho_m + 3p_m) \right) R \quad (15)$$

provided the cosmological term ρ_{Λ} is time dependent. If one assumes ordinary pressureless matter as

$$\rho_m = \rho_{m0}R^{-3} \quad (16)$$

where ρ_{m0} is the present density of matter. Then equation (13) will lead to the result that, the cosmological term will be independent of time. On the other hand this shows that the time dependent cosmological term does not decay in to pressureless matter.

Let us assume that the cosmological term can possibly decay into some form of matter with equation of state $p_m = \omega_m \rho_m$, where the parameter ω_m is assumed to be in the range $0 \leq \omega_m \leq 1$, the exact value depend on the particular matter component which is being created. In this paper we are considering only one component of matter. The covariant conservation law (8) can now be written for the possibility of cosmological term decaying into matter as

$$\frac{d\rho_m}{dt} + 3H(1 + \omega_m)\rho_m = -\frac{d\rho_{\Lambda}}{dt} \quad (17)$$

Since density behavior of ordinary pressureless matter does not work for a varying cosmological dark energy, we will assume the form for ρ_m which is slightly different from its canonical form, as [16, 17]

$$\rho_m = \rho_{m0} R^{-3+\delta} \quad (18)$$

where ρ_{m0} is the present value of ρ_m and δ is a parameter which is effectively depends upon the state of the universe. From equation (18) and (9), equation (17) become,

$$\rho_\Lambda \left(\frac{HR_h - 1}{HR_h} \right) = \left(\frac{3\omega_m + \delta}{2} \right) \rho_m \quad (19)$$

where we have assumed a vanishing integration constant and also with the condition that limit $t \rightarrow \infty$, $R(t) \rightarrow \infty$ and equation for time rate of horizon can be cast into the differential form

$$\frac{dR_h}{dt} = HR_h - 1. \quad (20)$$

Equation (19) suggest that, depending on the parameters δ and ω_m the energy densities ρ_m and ρ_Λ may eventually be of the same order, as suggested by the present observations [18]. This relation also gives the relation between dark energy and matter. When $\delta = 3$, the equation implies a constant matter density which corresponds to an equilibrium between matter creation and expansion of the universe.

In general event horizon is not exist in Friedmann universe. But in de Sitter universe there exists a event horizon, which satisfies the relation $R_h \sim H^{-1}$. Consequently for de Sitter universe, $HR_h \sim 1$ which implies that in de Sitter phase the energy density is almost completely dominated by the cosmological term or dark energy. For Friedmann universe we will hence take HR_h as a very large value. In general we will take the value of HR_h is equal to one or large.

3.1 Friedmann Universe

Friedmann universe is a homogeneous and isotropic universe, satisfying the conditions (14) and (15). With the relation between decaying cosmological term and created matter (19), the second Friedmann equation becomes,

$$\frac{d^2 R}{dt^2} = \frac{((1 + 3\omega_m) \beta^2}{2} \left[\frac{3\omega_m + \delta}{1 + 3\omega_m} \left(\frac{HR_h}{HR_h - 1} \right) - 1 \right] R^{\delta-2} \quad (21)$$

where $\beta^2 = 8\pi G\rho_{m0}/3c^2$. For de Sitter phase the acceleration is very large, for which $HR_h \sim 1$. As it enters the Friedmann phase by the decay of cosmological term or the dark energy, the acceleration can be negative or positive, which depends on the value of the term in the parenthesis of the right hand side of the above equation. The condition for acceleration is,

$$\frac{3\omega_m + \delta}{3\omega_m + 1} > 1 - \frac{1}{HR_h} \quad (22)$$

The factor $1 - \frac{1}{HR_h}$ is in the range $0 \leq 1 - \frac{1}{HR_h} \leq 1$. The extreme limits are corresponds to de Sitter phase and matter dominated universes respectively. For the transition period from de Sitter phase to Friedmann phase, HR_h is near to one, and assuming that the created matter have the equation state $\omega_m = \frac{1}{3}$, where the created matter is in relativistic form then

$$\delta > 2\alpha - 1 \tag{23}$$

where $\alpha = 1 - \frac{1}{HR_h}$ having value less than one. This implies that during the period of decay of the cosmological dark energy term the density of created matter is diluted slowly as the universe expand, and this decrease is faster than the decreasing of the density of non-relativistic matter in the Friedmann universe. This shows that even in the Friedmann universe it is possible to have an initial accelerating phase, where the cosmological dark energy is start its decay into matter and is still dominating over matter. As universe proceeds, the created matter will subsequently dominate and hence the universe will come to a matter dominated phase, at which the universe is expanding with deceleration.

For decelerating expansion, where matter is dominating over the cosmological term, the condition in the limit where HR_h is very large is,

$$\delta < 1 \tag{24}$$

This condition is true irrespective of whether the created matter is relativistic or non-relativistic. However as the universe enter the decelerating phase, the matter will become non-relativistic, satisfying the extreme condition that $\delta \rightarrow 0$ so that $\rho_m \sim R^{-3}$

3.2 Flat Universe

For flat universe, where the curvature parameter $k = 0$, the Friedmann equation (14) become

$$\left(\frac{dR}{dt}\right)^2 = \beta^2 \left(\frac{3\omega_m + \delta}{2} \frac{HR_h}{HR_h - 1} + 1\right) R^{\delta-1} \tag{25}$$

On integration and avoiding the integration constant, the solution is,

$$R \sim t^{\frac{2}{3-\delta}} \tag{26}$$

By considering the relation for matter creating out of decaying dark energy, i.e. $\rho_m = \rho_{m0}R^{-3+\delta}$, Then the relation between dark energy density and matter evolves as

$$\rho_m \sim \rho_\Lambda \sim t^{-2} \tag{27}$$

This is the time dependence of ρ_Λ for any value of ω_m and δ . This time dependence shows that ρ_Λ diverge at the initial time, which implies the existence of initial singularity.

3.3 An equation of state for the decaying dark energy

An equation of state for the time decaying cosmological term can be written as [19]

$$\omega_{\Lambda}^{eff} = -1 - \frac{1}{3} \left(\frac{d \ln \rho_{\Lambda}}{d \ln R} \right) \quad (28)$$

With the equation for the relation between decaying dark energy and creating matter [19], the equation of state become

$$\omega_{\Lambda}^{eff} = -\frac{\delta}{3} - \frac{1}{3(HR_h - 1)^2} \quad (29)$$

This shows that for large values of HR_h the equation of state become $\omega_{\Lambda} = -\frac{\delta}{3}$. From the above analysis, it is seen that for an accelerating universe ω_{Λ} is less than $-\frac{1}{3}$, but for a decelerating Friedmann universe it is greater than $-\frac{1}{3}$, which is similar to the latest analysis by many.

4. DISCUSSION

In the presence of a time varying cosmological term, assumed to be of holographic dark energy form, it is possible that the universe may begin with the de Sitter phase, exhibiting horizon and where the energy density is completely dominated by the dark energy. If the horizon R_h is assumed to be equal to the plank length at very early stage, then Λ , the cosmological constant would have a value of the order

$$\Lambda \sim 10^{66} \text{ cm}^{-2} \quad (30)$$

the corresponding dark energy density would be $\rho_{\Lambda} \sim 10^{112} \text{ erg cm}^{-3}$. This enormous dark energy decay into matter as the universe evolves to the Friedmann phase, and the dark energy reached the present value

$$\rho_{\Lambda}^0 = 10^{-8} \text{ erg cm}^{-3} \quad (31)$$

The evolution of the de Sitter phase into the Friedmann universe is in such a way that the total energy density comprising the dark energy, created matter and the gravitational field together be conserved. In this paper we have considered the decay of the dark energy into matter. During the initial phase of decay, the universe might be in the accelerating phase, where the parameter δ characterizing the equation $\rho_m \sim R^{-3+\delta}$, is greater than one. This implies that the dilution of the density of the created matter is slower compared to the non-relativistic matter. As the universe proceeds with expansion, the matter created will come to dominate, and the universe eventually go over to matter dominated phase, with the condition $\delta < 1$. In the extreme limit this condition may go the limit $\delta \rightarrow 0$, which emphasizes that, the created matter will eventually become non-relativistic, with behavior, $\rho_m \sim R^{-3}$. In section 3.3, the equation of the state of the decaying holographic dark energy is given and it shows that, in the early phase of universe too, $\omega_{\Lambda} < -\frac{1}{3}$ as

like the equation of state in late accelerating universe [20]. To explain why ρ_Λ and ρ_m are of the same order today, it is essential to have a specific time evolution for dark energy. We argued that a dynamical dark energy, endowed with an appropriate time evolution can contain the possibility of the development of a Friedmann universe from a de Sitter universe. As the de Sitter phase evolves to the Friedmann universe, the value of the dark energy is decreased gradually to a low value, which eventually leads to matter dominating phase with decelerating expansion. But on the other hand, recent observations indicating that the present universe is in a accelerating expansion phase. This fact indicates the possibility that at present the dark energy is increasing at the expense of decaying matter. This time increasing dark energy, in other words, implies that the universe may evolves in to state where the whole energy density would dominate completely by the dark energy. The ultimate clarity regarding these, of course be given by the proper analysis on the quantum effects, which is still an open question.

References

- [1] Perlmutter, S. et al.: Measurements of Omega and Lambda form 42 High-redshift supernovae, *Astrophys. J.* **517** 565 (1999)
Knop, R. et al.: New Constraints on Ω_M , Ω_Λ , and ω from an independent Set of Eleven High-Redshift Supernovae observed with *Astrophys. J.* **598** 102 (2003) [SPIRES]
Riess, A. G. et al.: Type Ia Supernovae Discoveries at $Z > 1$ From the Hubble Space telescope Evidence of Past Deceleration and Constraints on Dark Energy Evolution *Astrophys. J.* **607** 665 (2004) [SPIRES]
Jassal, H., Bagla, J., and Padmanabhan, T. : Observational Constraints on Low Redshift Evolution of Dark Energy: How consistent are Different Observations *Phys. Rev.* **D 72** 103503 (2005) [SPIRES]
- [2] Ratra, B., Peebles, P. J. E. : Cosmological Consequences of a Rolling Homogeneous Scalar field *Phys. Rev.* **D 37** 3406 (1998) [SPIRES]
Zlatev, I., Wang, L., Steinhardt, P. J. : Quintessence, Cosmic Coincidence and Cosmological Constant *Phys. Rev. Lett.* **82** 896 (1999) [SPIRES]
Steinhardt, P. J., Wang, L., Zlatev, I. : Cosmological Tracking Solutions 1999 *Phys. Rev.* **D 59** 123504 (1999) [SPIRES]
- [3] Weinberg, S. : Rev. Mod. Phys. The Cosmological Constant Problem, **61** 1 (1989)
- [4] Linde, A. : Particle Physics and Inflationary Cosmology, Harwood, New York, 1990.
- [5] Hsu, S.D.H. : Entropy bounds and dark energy, *Phys. Lett.* **B 594** 13 (2004) [hep-th/0403052] [SPIRES].
- [6] Li, M. : A model of holographic dark energy, *Phys. Lett.* **B 603** 1 (2004) [hep-th/0403127] [SPIRES];
- [7] . Huang, Q.-G., Li, M. : Anthropic principle favors the holographic dark energy, *JCAP* **03** 001 (2005)[hep-th/0410095] [SPIRES];
Huang, Q. -G., Li, M : The holographic dark energy in a non-at universe, *JCAP* **08** 013 (2004) [astro-ph/0404229] [SPIRES];
Chen, B., Li, M., Wang, Y. : Ination with Holographic Dark Energy, *Nucl. Phys.* **B 774** 256 (2007) [astro-ph/0611623] [SPIRES];
Zhang, J.-f., Zhang, X., Liu, H.-y.: Holographic dark energy in a cyclic universe, *Eur. Phys. J. C* **52** 693 (2007) [arXiv:0708.3121] [SPIRES]

Decaying Dark Energy and Emergence of FRW Universe

- Nojiri, S., Odintsov, S.D.: Unifying phantom inflation with late-time acceleration: Scalar phantom-non-phantom transition model and generalized holographic dark energy, *Gen. Rel. Grav.* **38** 1285 (2006) [hep-th/0506212] [SPIRES].
- [8] Horava, P., Minic, D. : Probable values of the cosmological constant in a holographic theory, *Phys. Rev. Lett.* **85** 1610 (2000) [hep-th/0001145] [SPIRES].
- [9] Horvat, R. : Holography and variable cosmological constant, *Phys. Rev. D* **70** 087301 (2004) [astro-ph/0404204] [SPIRES].
- [10] Aldrovandi, R., Beltrán Almeida, J.P., Pereira, J.G. : Time-Varying Cosmological Term: Emergence and Fate of a FRW Universe, *Grav. Cosmol.* **11** 277 (2005) , arXiv:gr-qc/0312017v3 12 Apr 2005.
- [11] Ratra, B., and Peebles, P.J.E. : Cosmological Consequences of a Rolling Homogeneous Scalar field *Phys. Rev. D* **37** 3406 (1998) [SPIRES]
- [12] Friman, J., Hill, C.T., Watkins, R. : Late Time Cosmological Phase Transitions, I. Particle Physics Models and Cosmic Evolution *Phys. Rev. D* **46** 1226 (1992)
- [13] Sahni, V., Starobinsky, A.A. : The Case for a Positive Cosmological Lambda-term *Int. J. Mod. Phys. D* **9** 373 (2000) .
- [14] Huang, Q.-G., Li, M. : Holographic Dark Energy in Non-Flat Universe *J. Cosmol. Astropart. Phys.* JCAP **0408** 013 (2004) [SPIRES]
- [15] Mashhoon, B., Wesson, P.S. : Gauge Dependent Cosmological Constant *Class. Quant. Grav.* **21**, 3611 (2004)
- [16] B.Guberina, R.Horvat and Hrvoje Nikolic, Non-Structured Holographic Dark Energy, *JCAP* **0701** (2007) 012
- [17] B.Guberina, R.Horvat and Hrvoje Nikolic, Dynamical Dark Energy with a constant vacuum energy density, *Phys. Lett. B* **636**: (2006) 80-85
- [18] S M Carroll, why is the universe Accelerating, in - Measuring and modelling the universe. ed. by W.L.Freeman, Cambridge University Press, Cambridge, 2003 [astro-ph/0310342]
- [19] C J Fang, Holographic Cosmological Constant and Dark Energy, *Phys. Lett.* **B663** (2008) 367.
- [20] E J Copeland, M Sami, S Tsujikawa, Dynamics of Dark Energy, *Int. J. Mod. Phys. D* **15** (2006) 1753
- [21] S.Weinberg, Gravitation and Cosmology, Wiley, New York, 1972

Grain Size Dependent Photo Luminescent Studies on Nanostructured Zinc Oxide

Athira Sundaran¹, Biji V², Gokul A M², Neethu Sha A P³

¹Fourth Semester M. Sc. Physics, Government College for Women, Thiruvananthapuram-695034 India

²Fourth Semester B. Tech EEE, Government Engineering College, Thiruvananthapuram-695035 India

³Research Scholar, Government College for Women, Thiruvananthapuram-695034 India

Abstract: ZnO nanoparticles were synthesized using chemical precipitation technique. The characterization of the sample was done using XRD and optical study was done using PL spectra. From XRD it was found that the grain size decreased with increase in pH. The PL spectra exhibited excellent fluorescent characteristics of ZnO. The average bandgap of ZnO nanoparticles were also calculated at different excitation wavelengths. Comparative study of ZnO samples were done by varying pH and temperature. Vibrational spectra of the nanoparticles were recorded in the range 400-4000 cm⁻¹. The peaks of ZnO nanoparticles annealed at higher temperature were found to be weaker compared to those annealed at lower temperature.

Keywords: nanomaterials, vibrational spectra, zinc oxide

1. INTRODUCTION

Nanotechnology and nanoscience are broad and interdisciplinary areas of research and development activity that have been growing explosively world wide during the past several years. It has the potential in revolutionizing the ways in which materials and products are created and the range and nature of functionalities accessed [1]. It is an interdisciplinary science that involves physics, chemistry, mathematics, and life sciences in particular genomics and proteomics. A nanometer is 1 billionth of a meter. In simple terms nanotechnology can be defined as engineering at very small length scales. Design, fabrication and application of nanostructures or nanomaterials and the fundamental understanding of the relationships between physical properties and materials dimensions characterize the fields of nanotechnology and nanoscience [2].

Nanostructured materials are materials with morphological features on the nanoscale, and especially those which have special properties stemming from their nanoscale dimensions [3]. When the dimension of a material is continuously reduced from a large macroscopic value to a very small size, the properties remain the same at first and then changes begin to occur. When the size drops below 100 nm, dramatic changes in properties can take place. If one dimension is reduced to the nanometer range while the other two dimensions remain large, the obtained structure is a quantum well. Two dimensional materials such as thin films and other engineered

surfaces are examples. If two dimensions are reduced and one dimension remains large, the resulting nanostructure is referred to as a quantum wire. Quantum wires include carbon nanotubes, nanowires, whiskers, etc. The limiting case of this process of size reduction is when all the three dimensions reach nanometer range. This process produces quantum dots. Fullerenes, dendrimers and other nanoparticles fall in this category.

Knowledge of variations in the properties of nanoparticles with particle size is important to the fundamental understanding of these systems and is also useful in a variety of technological applications. Spatial confinement can in general affect a property when the size of the system becomes comparable to or smaller than a critical length scale for the mechanism that is responsible for that property. The uniqueness of nanoparticles lies in its large surface to volume ratio. As the particle size decrease the spectral indicators and the characteristics of the surface atoms or ions become increasingly dominant. Also in nanostructured materials, when the crystal size is reduced to a few nanometers the average density and the coordination between the nearest neighbors are changed. As a result, the properties of these materials become different from those of bulk crystals.

Zinc oxide (ZnO) is a well-studied representative of II-VI class of semiconductors. It has a unique position among semiconducting oxides due to its piezoelectric and transparent conducting properties [4]. It has a wide band gap of 3.37 eV and large exciton binding energy of 60 meV. It has high electrical conductivity and optical transmittance in the visible region. These properties make it an ideal candidate for applications like transparent conducting electrodes in flat panel displays and window layers in solar cells. ZnO has applications in areas such as laser diodes, solar cells, gas sensors, and optoelectronic devices. It has a crystalline wurtzite structure, shown in Fig. 1.

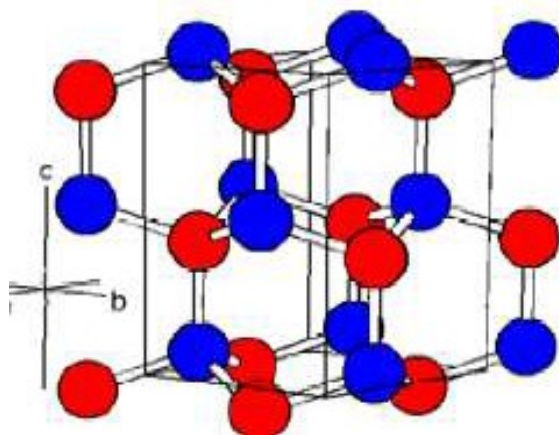


Fig.1: Wurtzite structure of zinc oxide (ZnO)

Experimental

Nanoparticles of ZnCO₃ were synthesized through controlled chemical reaction between solutions containing Zn²⁺ and CO₃²⁻ in presence of EDTA as the stabilizer. The reaction is $\text{Na}_2\text{CO}_3 + \text{Zn}(\text{NO}_3)_2 \rightarrow \text{ZnCO}_3 + 2\text{Na}(\text{NO}_3)$.

0.1Normal (N) Na₂CO₃ and 0.1N Zn(NO₃)₂ were taken in two conical flasks and were mixed with 100ml distilled water. Using two dropping funnels, the compounds were allowed to fall drop by drop into a vessel of 0.01N EDTA solution. The synthesis was carried out with the reaction mixture under constant stirring. The white gel like precipitate of nanoparticle ZnCO₃ was filtered, washed with distilled water and acetone several times to remove the impurities. ZnCO₃ sample was annealed at different temperatures to obtain samples of ZnO of different grain size. Five samples were prepared by changing the pH of the precursors, annealing temperature, etc. The sample codes, annealing time and temperature are given in the table below:

Sample code	pH	Annealing temperature (°C)	Annealing time (minutes)
S1	10	250	15
S2		300	15
S3		400	15
S4	8	300	15
S5		400	15

Table.1. ZnO nanoparticles synthesized by changing the pH of precursors and annealing temperature

RESULTS AND DISCUSSION

X ray diffraction patterns of nanoparticles of ZnO synthesized by changing the pH of the precursors and annealing temperature are shown in Fig.2 and Fig.3. Grain size (t) of each sample was calculated using Scherrer formula [5]

$$t = k\lambda/\beta\cos\theta \dots\dots\dots(1)$$

where k is a constant, λ is the wavelength of x-ray used, β is the full width at half maximum, θ is the scattering angle. The grain sizes calculated for the different samples are given in Table 2. They range from 12 to 24 nm.

A comparative study of ZnO nanoparticles synthesized by annealing at same temperature 300°C and 400°C but by varying pH was done. It was found that the grain size decreased with increase in pH. It is listed in the Table 3. The d spacing of each peak are calculated and listed with the X-Ray Diffraction (Fig.4). It revealed that the peaks of all the samples were consistent with the standard X-Ray Diffraction values of ZnO with Hexagonal structure (ICDD-79-0205). The plane of reflection of each peak can be determined using the standard X-Ray diffraction values. The hkl values are consistent with the standard values of ZnO.

The material ZnO shows fluorescence. From the photoluminescence spectra (Fig. 5-8) it is seen that the ZnO nanoparticles are effective fluorescent materials. The emission wavelength and intensity of the nanoparticles are listed in Table (4-7). The ZnO samples have fluorescent emission with wavelength between 380 nm to about 570 nm. This is in the visible region (380 nm to 750 nm). The main peaks of the emission spectra are at a wavelength of 465 nm (blue region 450 nm to 495 nm) and 448 nm (very near to the blue region). The excitation wavelengths are in the UV region. At excitation wavelength 360 nm, resonance fluorescence begins and they have high intensity at the excitation wavelengths 365 nm and 370 nm. At the excitation wavelength 365 nm, a peak with small intensity occurs with wavelength 730 nm (double of 365) and at 370 nm a peak with high intensity occurs with wavelength 740 nm (double of 370 nm). The intensity of all the peaks for the sample S5 (23.92 nm) is greater than the corresponding intensity of emission of sample S1 (12.66 nm). From the UV-Visible studies the average bandgap values corresponding to different excitation wavelengths were obtained and are listed in Table 8.

Fourier Transform Infrared Spectroscopy (FTIR) spectra of nanoparticles of ZnO (S1 and S2) at two different temperatures (250°C and 300°C respectively) are shown in Fig 9 and Fig 10. The presence of a small amount of adsorbed water in both the samples is indicated by the characteristic vibrational mode of O-H stretching and O-H bending. The intensity of these modes in the spectrum of the sample (S2) annealed at a higher temperature is weaker (Fig.10) compared to the sample (S1) annealed at a lower temperature (250°C) (Fig. 9). In the spectrum of nanoparticles of ZnO obtained by annealing the at 250°C, (S1), the characteristic lattice modes of ZnO are observed at 459 cm⁻¹ and 413 cm⁻¹. The positions of these peaks shifted to 436 cm⁻¹ and 420 cm⁻¹ respectively in the spectrum of the sample S2. The XRD results showed that the grain size of the ZnO nanoparticle samples annealed at 300°C is a little larger compared to that annealed at 250°C. Hence the shift of the peaks in the lattice mode region in the spectrum

shown in Fig.10 compared to the positions of the corresponding peaks in Fig. 9 can be due to the difference in the grain sizes of the two nanoparticles samples.

Samples	Average grain size (nm)
S1	12.66
S2	14.73
S3	21.40
S4	17.50
S5	23.92

Table 2. Grain size of ZnO nanoparticles synthesized by varying the pH and annealing temperature of the precursor

Samples	Temp ($^{\circ}$ C)	pH	Average Grain size (nm)
S4	300	8	17.50
S2		10	14.73
S5	400	8	23.92
S3		10	21.40

Table 3. Comparison of ZnO nanoparticles synthesized at (a) 300° C and (b) 400° C at two different pH

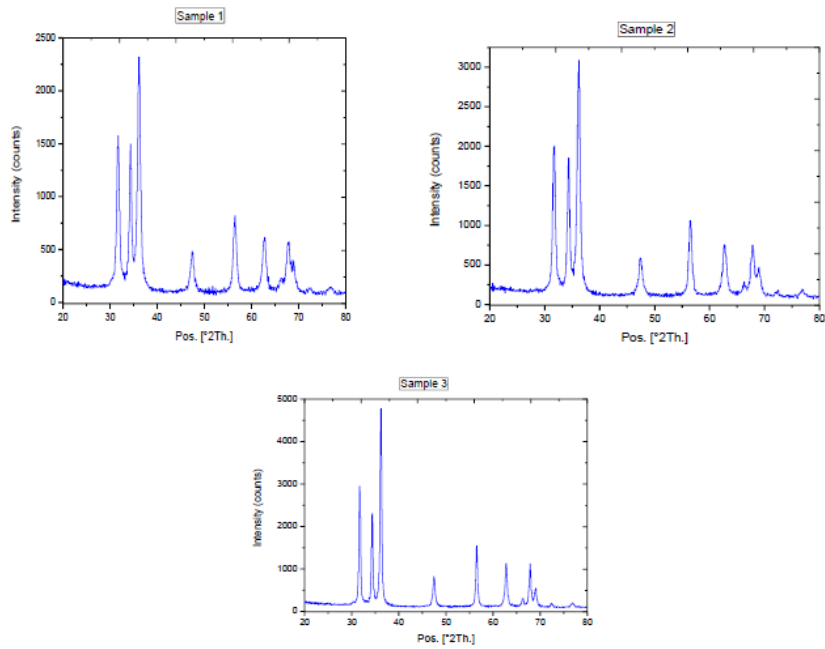


Fig. 2: XRD pattern of ZnO nanoparticles synthesized at pH value of 10 at annealing temperatures (a) 250°C (b) 300°C (c) 400°C

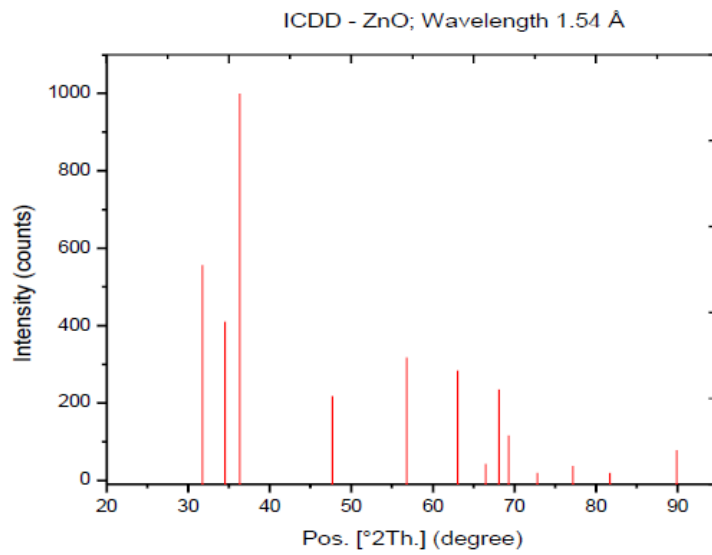


Fig.4: d-spacing of ZnO nanoparticles

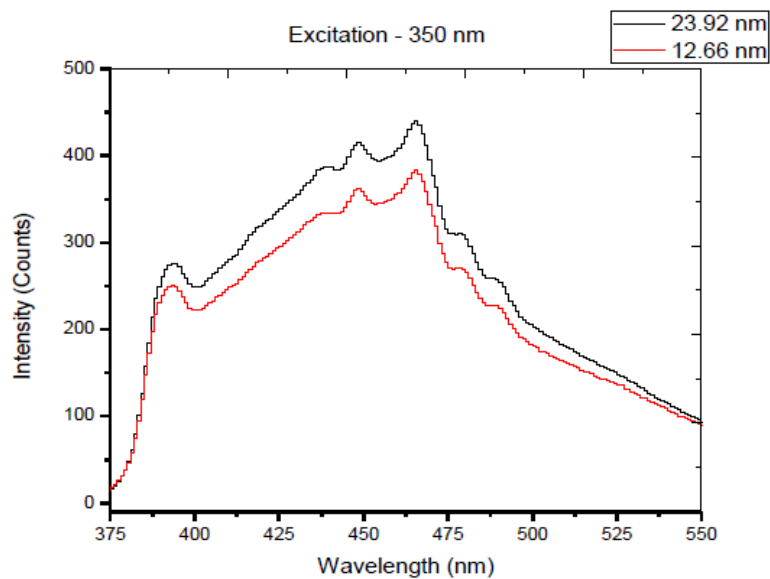


Fig.5: PL of nanoparticles of ZnO at excitation wavelength of 350 nm

Samples	Wavelength of emission (nm)	Intensity (counts)
S1(12.66 nm)	465	386
	448	366
	393	251
S5(23.92 nm)	465	439
	448	414
	393	278

Table.4: Emission wavelength and intensity of ZnO samples (S1 and S5) at 350 nm

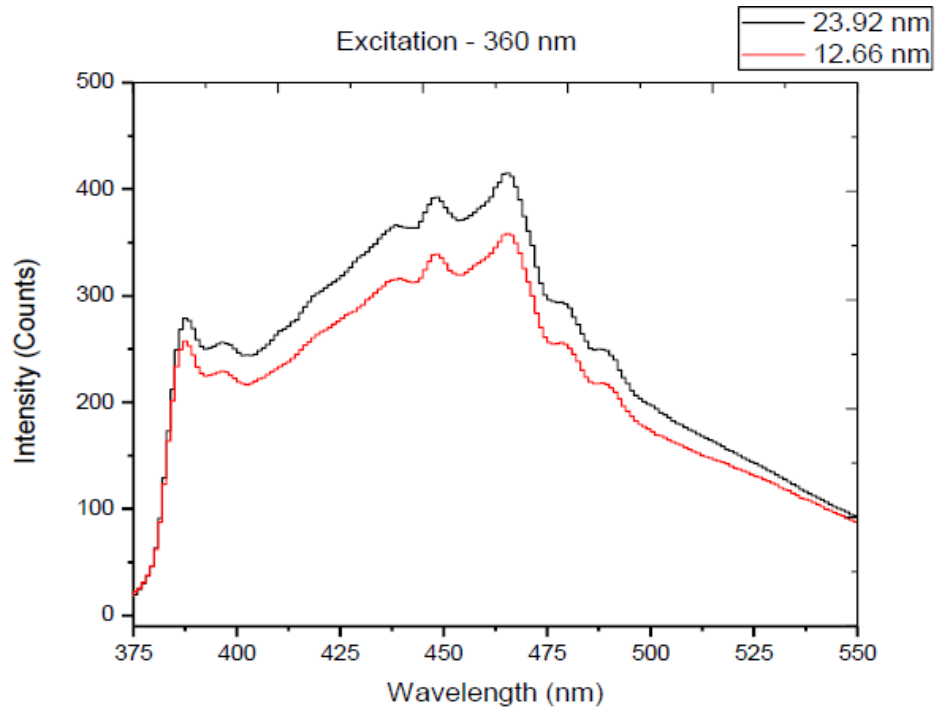


Fig.6: PL of nanoparticles of ZnO at excitation wavelength 360 nm

Samples	Wavelength of emission (nm)	Intensity (counts)
S1(12.66 nm)	465	356
	448	340
	387	253
	360	278
S5(23.92 nm)	465	414
	448	393
	387	278
	360	114

Table 5: Emission wavelength and intensity of ZnO samples (S1 and S5) at excitation wavelength 360 nm

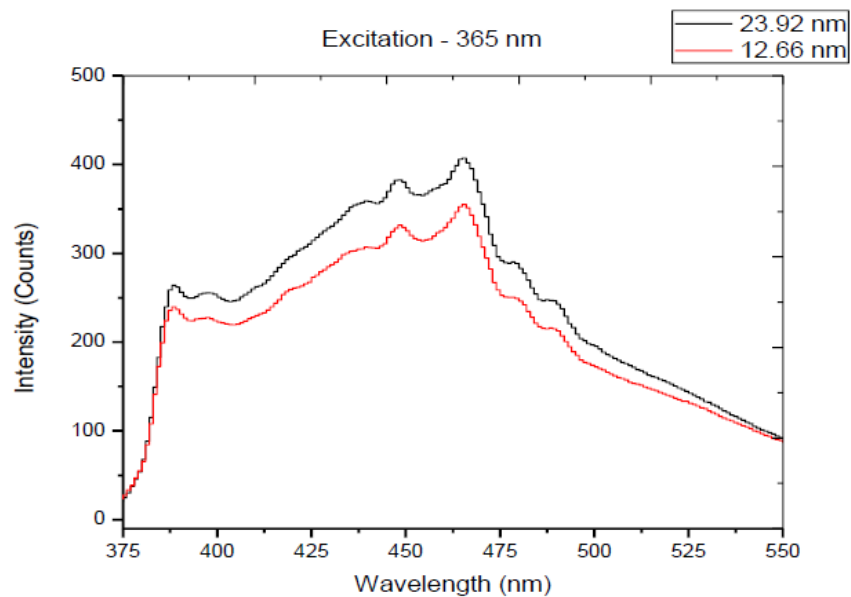


Fig.7. PL of nanoparticles of ZnO at excitation wavelength of 365 nm

Samples	Wavelength of emission (nm)	Intensity (counts)
S1(12.66 nm)	465	343
	448	324
	393	237
	370	High
	740	High
S5(23.92 nm)	465	402
	448	375
	393	267
	370	High
	740	High

Table 6: emission wavelength and intensity of nanoparticles of ZnO (S1 and S5) at excitation wavelength of 365 nm

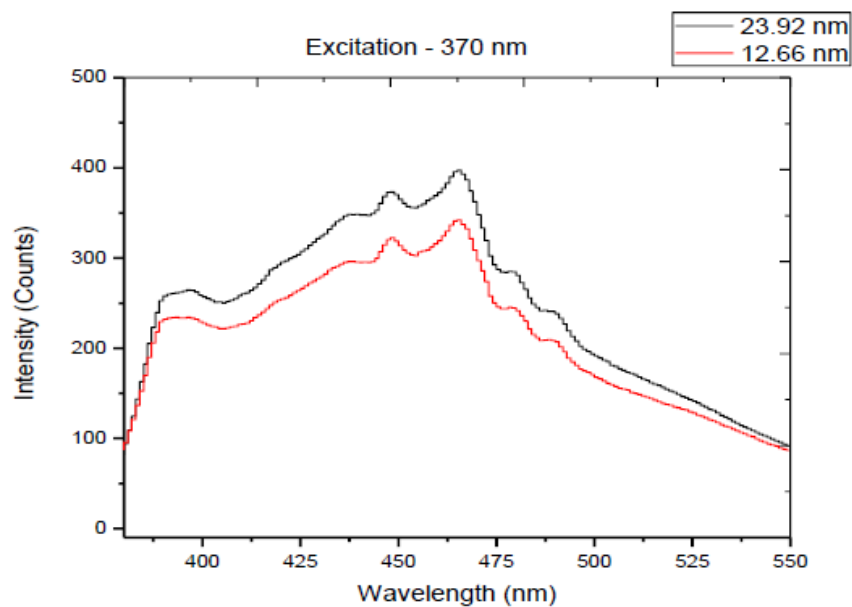


Fig.8. PL of nanoparticles of ZnO at excitation wavelength of 370 nm

Samples	Wavelength of emission (nm)	Intensity (counts)
S1(12.66 nm)	465	343
	448	324
	393	237
	370	High
	740	High
S5(23.92 nm)	465	402
	448	375
	393	267
	370	High
	740	High

Table 7: Emission wavelength and intensity of nanoparticles of ZnO (S1 and S5) at 370 nm

Sample Code	Excitonic peak position (nm)	Average Band gap (eV)
S1 and S5	350	2.84
	360	3.00
	365	2.73
	370	2.84

Table.8. Average bandgap of ZnO samples (S1 and S5) excited at different wavelengths

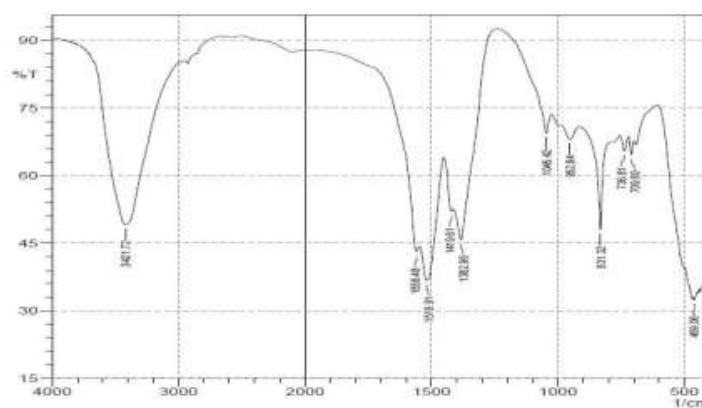


Fig.9. FTIR spectrum of nanoparticles of ZnO synthesized by annealing the precursor at 250°C

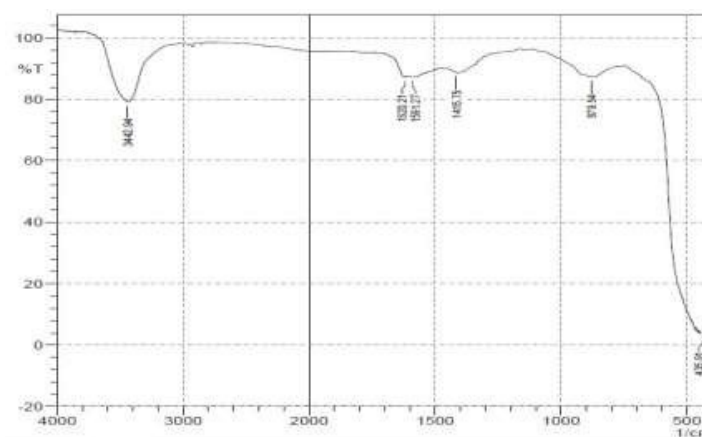


Fig.10. FTIR spectrum of nanoparticles of ZnO synthesized by annealing the precursor at 300°C

Conclusion

Crystalline ZnO with nanometer dimensions are synthesized. The X-Ray diffraction of the samples are taken and the grain sizes are calculated. It was observed that the grain size increases with increase in temperature at constant pH. It is also observed that the grain size decreases with increase in pH at constant temperature. From the detailed X-Ray diffraction study the crystal structure was determined by comparing the Joint Committee on Powder Diffraction Standards (JCPDS)-International Centre for Diffraction Data (ICDD) values. Zinc oxide nanoparticles show Hexagonal (Wurtzite) structure. The photoluminescence spectra of the samples with different grain sizes were compared. The intensity of fluorescent emission of samples with greater grain size was more than the samples with small grain size. There was no shift in the frequency of fluorescence emission for the samples with grain size 12.66 nm and 23.92 nm. This revealed that the effective fluorescent emission of Zinc Oxide lies in the blue region of electromagnetic spectrum. The FTIR spectra of nanoparticles of ZnO were recorded in the range 400-4000 cm⁻¹. It was found that the peaks of ZnO samples associated with O-H vibration mode of adsorbed water molecules, annealed at higher temperature were weaker compared to that annealed at lower temperature.

REFERENCES

- [1] Kumar, Narendra, and Sunita Kumbhat. Essentials in Nanoscience and Nanotechnology. John Wiley & Sons, 2016.
- [2] Cao, Guozhong. Nanostructures and nanomaterials: synthesis, properties and applications. World Scientific, 2004.
- [3] Buzea, Cristina; Pacheco, Ivan; Robbie, Kevin (2007). "Nanomaterials and Nanoparticles: Sources and Toxicity". *Biointerphases*. 2 (4): MR17-MR71. PMID 20419892
- [4] Ginley, D., & Bright, C. (2000). Transparent Conducting Oxides. *MRS Bulletin*, 25(8), 15-18. doi:10.1557/mrs2000.256
- [5] Patterson, A. (1939). "The Scherrer Formula for X-Ray Particle Size Determination". *Phys. Rev.* 56 (10): 978-982.
- [6] (a) Schneider, R.; Wolpert, C.; Guilloteau, H.; Balan, L.; Lambert, J.; Merlin, C. *Nanotechnology* 2009, 20, 225101. (b) Dumas, E.; Gao, C.; Suffern, D.; Bradforth, S. E.; Dimitrijevic, N. M.; Nadeau, J. L. *Environ. Sci. Technol.* 2010, 44, 1464.
- [7] Tang, Z.; Kotov, N. A.; Giersig, M. *Science* 2002, 297, 237.
- [8] (a) Xiong, H.; Xu, Y.; Ren, Q.; Xia, Y. *J. Am. Chem. Soc.* 2008, 130, 7522. (b) Moussodia, R. O.; Balan, L.; Merlin, C.; Mustin, C.; Schneider, R. *J. Mater. Chem.* 2010, 20, 1147.

STUDENT JOURNAL OF PHYSICS

Volume 6

Number 2

Apr - Jun 2017

CONTENTS

ARTICLES

Exploration of the Quantum Casimir Effect	75
A. Torode	
Solar wind and Sunspot variability in the 23rd and 24th solar cycles: A comparative analysis	83
M. Adhikary and P.K. Panigrahi	
Fourier Transform of Electric Signal using Kundt's Tube	95
S. Paul and M. C. Gandikota	
Decaying Dark Energy and Emergence of FRW Universe	101
Athira Sasidharan and Titus K Mathew	
Grain Size Dependent Photo Luminescent Studies on Nanostructured Zinc Oxide	110
Athira Sundaran, Biji V, Gokul A M, Neethu Sha A P	